DEVELOPMENT OF CATALYSTS FOR THE CONVERSION OF LIGHT ALKANES TO LIQUID FUEL HYDROCARBONS

by

Christian J. Breckner

A Dissertation

Submitted to the Faculty of Purdue University

In Partial Fulfillment of the Requirements for the degree of

Doctor of Philosophy

Davidson School of Chemical Engineering

West Lafayette, Indiana

August 2023

THE PURDUE UNIVERSITY GRADUATE SCHOOL

STATEMENT OF COMMITTEE APPROVAL

Dr. Jeffrey T. Miller, Chair

Davidson School of Chemical Engineering

Dr. Rajamani Gounder

Davidson School of Chemical Engineering

Dr. Jeffrey P. Greeley

Davidson School of Chemical Engineering

Dr. Christina W. Li

Department of Chemistry

Approved by:

Dr. John A. Morgan

Dedicated to my family and friends for their love and support

ACKNOWLEDGMENTS

The four years that I spent at Purdue University were highly transformative. The skills that I have learned and feedback I have received have molded me into an effective researcher. This would not have been possible without the support of several individuals.

I would like to express my appreciation to my advisor, Jeffrey T. Miller. His approach of tackling big picture issues by pursuing innovative solutions is something that I will carry with me as I transition to research in industry. His guidance and expertise opened the door for many collaborations with researchers across the globe. I would also like to thank my committee members Rajamani Gounder, Jeff Greeley, and Christina Li for providing insightful feedback that helped fine tune my research pursuits. Finally, this all would not have been possible without funding from the Davidson School of Chemical Engineering and CISTAR.

I would like to express my appreciation to the group members who helped make this work possible: from providing guidance as a new researcher to spending long, sleepless nights at the beamline collecting critical data, and everything in between. Thank you to the undergraduate and high school students that I had the pleasure to mentor. It has been amazing watching you grow into self-sufficient researchers. I would also like to express my gratitude to the collaborators that helped collect invaluable data for my research projects: Kuixin Xu and Christian Li for their help with STEM in chapter 2, Mingrui Wang and Guanghui Zhang for their help with IR in chapter 2, and Hien Pham and Abhaya Datye for help with STEM and EDS in chapter 3.

Finally, I would like to thank my family, friends, classmates, and most importantly my girlfriend for their support and encouragement throughout my Ph. D. experience.

TABLE OF CONTENTS

LIST OF TABLES

LIST OF FIGURES

ABSTRACT

The conversion of ethane and propane to liquid fuels is an invaluable process that will help bridge the energy gap from fossil fuels to renewable energy sources. The development of shale gas upgrading technology must be aggressively pursued in order to achieve this goal. This necessitates the discovery, development, and optimization of non-traditional catalysts for upgrading these light alkane species in a cost-effective manner.

In this thesis, two catalysts were studied for different reaction steps in light alkane upgrading: strong-metal support interaction (SMSI) catalysts were studied with a focus on improving dehydrogenation activity and γ-Al_2O_3 as a new, innovative type of Lewis acid catalyst for oligomerization. Strong metal-support interaction catalysts have shown to improve desired product selectivity at the cost of fractional rates due to active site coverage. The goal of the SMSI study was to determine if the active site coverage of metallic nanoparticles could be controlled to lower levels than previously reported in SMSI catalysts with the aim of improving the rate while maintaining high selectivity. 2Pd-XTi/SiO_2 (2 wt% Pd, X wt% Ti) SMSI catalysts were synthesized to control Pd nanoparticle coverage. Increasing the Ti loading from 0.1 to 1.0 wt% increased the surface coverage from 40 to 85% after 550 °C reduction. The SMSI overlayer was removed by oxidation at 350 °C and re-reduction at 200 °C. Increasing the reduction temperature from 300 to 550 °C increased the SMSI coverage from 10 to 85% depending on the Ti loading and temperature which is a significant improvement over the 70-95% coverages previously observed. Catalysts with excess coverage result in a decreased rate with no improvement on product selectivity. Lower coverages allow for rate and selectivity optimization. Reducing coverage can improve the rate without a significant loss to selectivity. The coverage at which this occurs will vary based on the catalyst and reaction network.

The goal of the second study was to identify the active sites for olefin oligomerization on γ-Al_2O_3 and to determine their density. XSr/Al_2O_3 (X wt% Sr) catalysts were synthesized to poison the active sites. There was a decrease in the propylene oligomerization conversion with increasing Sr loading with >95% conversion loss above 1 wt% Sr. Pyridine IR indicates only Lewis acid sites

on γ-Al_2O_3. There was a linear decrease in the intensity of the Lewis acid peaks in the IR spectra when increasing the Sr loading which correlates with the loss in propylene conversion suggesting that Lewis acid sites are the active site. The acid site density was calculated to be ~0.2 sites per nm^2 of γ-Al_2O_3. Lewis acid sites are not typical thought of as catalytic for many hydrocarbon reactions including olefin oligomerization. The techniques utilized in this work indicate that they are active. This opens opportunity to discover other Lewis acid catalysts which may be significantly more active. Discovery work to identify other Lewis acid catalysts, in particular single ion metals, is included in Chapter 4 with unexpected and promising results.

1. BACKGROUND

Recent discovery of large shale gas reserves in the United States combined with new production technologies including horizontal drilling and fracking have sparked a hydrocarbon revolution that has turned the country into a net hydrocarbon exporter. Horizontal drilling allows for the extraction of multiple shale gas deposits from significantly fewer wells. The extraction process is also significantly improved due to a more efficient flow geometry. Hydraulic fracking allows for the cracking of small formations near the wellbore which improves hydrocarbon extraction of shale gas deposits. Using both horizontal drilling and hydraulic fracking reduces the amount of fluid needed to extract hydrocarbons due to lower fluid velocity requirements and significantly lower pressure drops around the wellbore. These technological advancements have increased the supply of shale sourced hydrocarbons which opens opportunity in the refining and processing industries to upgrade shale gas species into value added products.

Shale gas consists of methane which is used for electricity and gas utilities. There are small amounts of other hydrocarbons, primarily ethane and propane, whose composition will vary by region and well. Ethane and propane are excellent feedstocks that can be used to create value added products; however, the industrial infrastructure and technology has not been developed for cost-effective processing of these chemicals at remote shale gas wells. Current technology consists of two independent processes: the formation of olefins from light alkanes and olefin conversion.

Traditional olefin producing processes include steam cracking, catalytic cracking, and more recently propane dehydrogenation. Historically, steam crackers utilize naphtha as a feedstock, a flammable liquid hydrocarbon mixture produced from natural gas and petroleum. Naphtha is treated at 800-870 °C and ~1.5 bar with steam which cracks large hydrocarbons into ethylene, propylene, and aromatics. With the increased production of shale gas, steam crackers in the United States have switched to ethane feed to produce ethylene. Fluid catalytic crackers in refineries utilize high molecular weight crude oils as a feedstock which are broken down into propylene, butylene, and high octane gasoline blendstocks. These units operate at 480-550 °C and ~1 bar with Y zeolite catalysts, but increased propylene yields can be obtained by adding

ZSM-5 zeolite. With the newfound availability of large amounts of propane from shale gas, propane dehydrogenation (PDH) plants are under construction to selectively produce propylene. PDH units operate at 500-600 °C and ~1.5 bar. Typical PDH catalysts include supported Pt or Pt alloys (typically on alumina) and chromia-alumina. These catalysts are highly selective and have high rates but suffer from deactivation and short catalyst lifetimes.

The olefins produced from dehydrogenation processes can serve as a feedstock for additional catalytic processes such as oligomerization which converts olefins into higher molecular weight products for fuels and chemicals. Oligomerization processes typically use ethylene, propylene, and butene as feedstocks. There are two types of catalysts commonly used in industry: metal alkyl and Brønsted acid catalysts. Metal alkyl catalysts are typically homogeneous catalysts that operate at 100 °C and >20 bar. A low temperature is required to prevent reduction to metal nanoparticles and loss of activity. Metal alkyl catalysts are highly efficient at producing linear alpha olefins (LAOs) which are utilized as surfactants and lubricants but are not suitable for gasoline blendstocks. Olefin oligomerization also occurs on Brønsted acid catalysts which are heterogeneous catalysts, most commonly ZSM-5. These typically operate at 250-400 °C and ~1 bar. Zeolites give a different product distribution than metal alkyls. Starting from ethylene (C2), metal alkyls will produce primarily linear, even carbon number terminal olefin products. Zeolites, however, not only oligomerize olefins, but also catalyze isomerization and cracking to produce every carbon number from about C4-C12 range depending on the feed and operating conditions. Low conversion (<40%) result in large chain olefin products due to oligomerization, isomerization, and disproportionation while higher conversions result in large chain olefins and aromatic products due to oligomerization, isomerization, disproportionation, and aromatization. This product range makes ZSM-5 extremely effective at forming liquid fuel products; however, it deactivates after only one week while other zeolites deactivate much more quickly. The large influx of light olefin species from the dehydrogenation of shale gas olefins necessitates the development of alternative oligomerization catalysts that are highly effective at producing liquid fuels.

Chapter 2 focuses on the development of strong metal-support interaction (SMSI) catalysts. SMSI is a phenomena where, at high temperature under reducing conditions, the support surface

migrates and covers the supported metallic nanoparticles. This process leads to a decrease in activity; however, for some reactions the selectivity is significantly improved. The goal of this study is to determine if the surface coverage of the metallic catalyst can be controlled leading to higher rates while maintaining the improved selectivity. It will be shown that SMSI can be utilized with existing PDH catalysts to improve selectivity and lifetime through optimization of its coverage using key synthesis and pretreatment techniques. The addition of small amounts of SMSI species can help to stabilize catalysts resulting in improved selectivity and catalyst lifetime at the cost of reduced rates due to active site coverage. Previous SMSI work has observed coverage of >70%; however, the benefits of SMSI may persist at lower coverage levels. Thus, it is important to understand what catalyst properties and treatments can be used to reduce coverage for optimization of SMSI catalysts.

Recently, γ-Al_2O_3 was shown to be catalytic for olefin oligomerization. Since γ-Al_2O_3 is well known to have only Lewis acid sites, these were proposed to be the catalytic site however, Lewis acid sites are not currently known to catalyze olefin oligomerization. The goal of the study in Chapter 3 was to determine the catalytic site on γ-Al_2O_3 for olefin oligomerization and to develop a method to determine the active site density. By poisoning the catalytic activity with Sr species, it is shown that the active site on γ-Al_2O_3 for oligomerization are Lewis acid sites. STEM and XAS characterization indicate that Sr is present as isolated ions on the support. From the linear loss in catalytic activity with added Sr ions, the number of catalytic sites can be estimated.

With the confirmation that Lewis acid sites on γ-Al_2O_3 catalyze olefin oligomerization, the catalytic properties of other potential Lewis acid catalysts were investigated. Chapter 4 reports preliminary results and identifies several new catalyst opportunities.

2. CONTROLLED SITE COVERAGE OF STRONG METAL-SUPPORT INTERACTION (SMSI) ON PD NP CATALYSTS[1]

2.1 Introduction

Since the original report of strong metal-support interaction (SMSI) by Tauster, et al. where a 2 wt% Pd/TiO_2 catalyst initially reduced at 175 °C experienced a significant drop in CO uptake when further reduced at 500 °C[2], there has been continued interest in utilizing this phenomenon for improving catalyst performance. SMSI has been shown to improve product selectivity, catalyst lifetime, and process performance in reactions such as propane dehydrogenation[3], olefin and acetylene hydrogenation[4-6], Fischer Tropsch synthesis[7], the water gas shift reaction[8], and in electrocatalysis[9]. Dulub and coworkers used electron microscopy on a Pt/TiO_2 catalyst to better understand why SMSI occurs. It was observed that the TiO_2 support, after surface species mobilization and partial reduction[10], covered metal nanoparticles resulting in less active sites available for catalysis[11]. Further work by Tauster, et al. found that this coverage could be reversed under high temperature oxidation[2]. Related work found that the same process can occur on Pt/CeO_2 catalysts as well indicating that this effect is not strictly limited to TiO_2 supports[12]. Further studies on transition metal oxide supports revealed that SMSI can occur on most reducible metal oxide supports such as TiO_2[9], CeO_2[12,13], Fe_3O_4[14,15], La_2O_3, Nb_2O_5[16], MnO_2[17], and even partially modified supports such as Tantalum-doped TiO_2[8]. SMSI has also been observed on non-reducible metal oxide supports such as ZnO[18,19] and non-metal supports such as hydroxyapatite[20,21] and Boron Nitride[22] through different migration and coverage processes. The metal nanoparticles that facilitate SMSI are as varied as the supports that induce them: Pd[2], Pt[11,12], Ag[23], Au[20], Ni, Fe[22], Rh[7,24], and Co[25], among others. Many early studies have concluded that the covered nanoparticles experience an electronic interaction with the encapsulating SMSI oxides[2,7,26-28]. Recent studies suggest that SMSI is primarily a physical interaction where the uncovered active sites do not experience an electronic interaction with the nearby SMSI oxide species[3,29-31]. It is likely that this misunderstanding of strong electronic interactions arose due to reactive metal-support interactions

(RMSI), a process in which the encapsulating SMSI oxide becomes fully reduced to form an alloyed nanoparticle which experiences electronic interactions[32].

While studies on SMSI oxide supports were useful in understanding the encapsulation process, they have been shown to display low activity, particularly at reaction temperatures of 500 °C and above as the metal active sites become covered to near completion. Addition of low loadings of SMSI oxides to catalysts on inert supports, e.g. Pt-Ti/SiO_2, also display lower chemisorption and catalytic activity at these high reaction temperatures[3,5,16]. Previous studies have typically used SMSI oxide loadings of greater than 1 wt%. While these have improved rates compared to nanoparticles on SMSI supports and retained the benefits of increased selectivity, improved catalyst lifetime, and reduced leaching rates in liquid systems[3,25], the rates remain relatively low compared to catalysts without SMSI oxides. Other methods, such as atomic layer deposition (ALD) of metal oxides onto supported metal nanoparticles, have the same effect seen in these SMSI systems[25,30,33]. For both SMSI and ALD catalysts the loss of nanoparticle surface coverage is typically greater than 70%. Lower surface coverage may give desirable modifications to catalytic performance but at higher rate. Currently, however, there are no methods to control the SMSI surface coverage levels below 70%.

In the present work, the goal was to determine if the active site coverage of metallic nanoparticles could be controlled to lower levels than have been previously reported in SMSI catalysts with the aim of improving the rate while maintaining high selectivity. Several methods are given to control the $TiO_{(2-x)}$ SMSI coverage of Pd nanoparticles from 10 to 80%. CO chemisorption, propylene hydrogenation rates, CO IR spectroscopy, STEM, and *in situ* X-ray absorption spectroscopy (XAS) are combined to show that the catalytic surface of ~2 nm sized Pd particles in 2Pd-XTi/SiO_2 sequentially impregnated SMSI catalysts (2 wt% Pd, X wt% Ti, SiO_2 support) become partially covered by SMSI oxides in a controllable manner. A method to determine the fractional Pd surface coverage is also provided.

2.2 Materials and Methods

2.2.1 Materials

Davisil 636 silica (99%), titanium(IV) bis(ammonium lactato)dihydroxide (50% solution), and tetraamminepalladium(II) nitrate (10% solution) were purchased from Sigma-Aldrich. All gases used for catalytic testing were purchased from Indiana Oxygen Company. 3% C_3H_6 and 5% H_2 were both balanced with N_2. The gases for XAS experiments were 3% H_2 balanced in He, pure He, and 10% O_2 balanced in He. All gases for XAS were purchased from AirGas, Illinois.

2.2.2 Catalyst Preparation

The control, non-SMSI $2Pd/SiO_2$ catalyst (0 wt% Ti, 2 wt% Pd) was synthesized using pH adjusted incipient wetness impregnation (IWI) on Davisil 636 silica (pore size = 60 Å, surface area = 480 $m^2\ g^{-1}$). Ammonium hydroxide was added dropwise to a 10 wt% $Pd(NH_3)_4(NO_3)_2$ solution diluted in deionized water until the pH was 11. This solution was added dropwise to Davisil 636 silica. The catalyst was dried overnight at 125 °C, split into thirds, and calcined at 450/600/700 °C for 3 hours each. The three catalysts were reduced in 5% H_2/N_2 (~100 mL min^{-1}) at 200 °C for 30 minutes and 250 °C for 30 minutes.

2Pd-XTi/SiO_2 (denoted as X wt% Ti containing catalyst throughout this paper, 2 wt% Pd) sequentially impregnated strong metal-support interaction (SMSI) were synthesized using sequential incipient wetness impregnation (IWI). Varied amounts of titanium(IV) bis(ammonium lactate) dihydroxide (50% solution) corresponding to 0.1/0.5/1.0 wt% Ti were diluted in deionized water and added dropwise to Davisil 636 silica. The XTi/SiO_2 catalyst precursors were dried overnight at 125 °C and calcined at 300 °C for 3 hours. A second solution containing 10 wt% tetraamminepalladium(II) nitrate solution diluted in deionized water was pH adjusted to 11 using ammonium hydroxide. This solution was added dropwise to the XTi/SiO_2 catalyst precursors to achieve a loading of 2 wt% Pd. The 2Pd-XTi/SiO_2 catalysts were dried overnight at 125 °C, split into thirds, and calcined at 450/600/700 °C for 3 hours each. The resulting 12 2Pd-XTi/SiO_2 catalysts were sequentially reduced in 5% H_2/N_2 (~100 mL min^{-1}) at 200 °C for 30 minutes and 250 °C for 30 minutes. SMSI was induced on the 2Pd-XTi/SiO_2 catalysts prior to analysis using a

pre-treatment reduction temperature of 550 ℃ to initially stabilize particle sizes. The SMSI overlayer was removed using oxidation at 350 ℃ for 30 minutes. Analysis of the non-SMSI state was possible using a re-reduction temperature of 200 ℃ which did not induce SMSI coverage.

2.2.3 CO Chemisorption

CO chemisorption was performed on a Micromeritics ASAP 2020 chemisorption instrument using a volumetric chemisorption analysis to determine relative particle sizes. A U-shaped quartz tube was filled with approximately 0.1 g of catalyst. The samples for the $2Pd/SiO_2$ (0 wt% Ti) catalysts were reduced in 5% H_2/He at temperatures ranging from 250-550 ℃ for 30 minutes prior to analysis at 30 ℃. The 0.1-1.0 wt% Ti containing catalyst samples were reduced in 5% H_2/He at 250 ℃ for 30 minutes. The 250 ℃ pre-treatment was used to determine if the SMSI catalysts had the same changes to relative particle size as the $2Pd/SiO_2$ (0 wt% Ti) catalyst when increasing the calcination temperature. CO uptakes were estimated by taking the difference between the physisorption plus chemisorption and the physisorption only uptakes at different pressures. A linear regression of these points was used to estimate the uptake at zero pressure in mmol CO/g metal. The sample loading and Pd wt% were used to convert to mol CO/mol metal. Pd nanoparticles can bind CO in a linear, bridging, or three-fold manner depending on the nanoparticle size. Larger Pd nanoparticles (> 4 nm) have predominately bridge bonding and three-fold bonding while small nanoparticles (< 4 nm) have a mixture of linear, bridge, and three-fold bonding. Higher reduction temperatures result in larger particle sizes and more face sites which cause the bonding factor to increase. This changing bonding factor makes it difficult to estimate particle sizes directly using only CO chemisorption.

2.2.4 Propylene Hydrogenation Catalytic Performance Tests

Propylene hydrogenation TORs at 30 ℃ were used to compare the performance of the catalysts. Rate measurements of the non-SMSI state were used in conjunction with Pd EXAFS dispersion estimates to calculate the TORs of all catalysts. The $2Pd/SiO_2$ (0 wt% Ti) catalyst was reduced at 250-550 ℃ then the rate was measured at 30 ℃. For these reaction tests the 0.1-1.0 wt% Ti containing catalysts were reduced at 550 ℃, oxidized at 350 ℃, then re-reduced at 200-550 ℃. The change in catalytic rate from the SMSI state (re-reduced between 300-550 ℃) to the non-

SMSI state (re-reduced at 200 °C) after the initial 550 °C reduction to stabilize particle size was used to estimate particle coverages. All catalytic tests were performed in a 12.7 mm ID quartz tube fixed bed reactor with a K-type thermocouple placed in the center of the bed to monitor the reaction temperature. A furnace connected to a temperature controller was used to manually adjust the bed temperature. Approximately 10 mg of catalyst was loaded into the reactor and was diluted to 1 g using SiO_2. The reactions were performed in 2.0% H_2 and 1.8% C_3H_6 balanced with N_2 at 30 °C. The products were analyzed using a Hewlett Packard 6890 GC with a flame ionization detector (FID). Peaks were integrated and compared to a bypass run of the mixed gases to determine conversion and catalytic rate. The catalytic rate was calculated using the conversion and initial propylene flow rate to obtain mol $C_3H_8*g_{cat}^{-1}*s^{-1}$. The catalyst loading and Pd wt% were used to transform this to mol $C_3H_8*mol_{metal}^{-1}*s^{-1}$. The TOR was calculated by dividing the catalytic rate in mol $C_3H_8*mol_{metal}^{-1}*s^{-1}$ by the dispersion from EXAFS. Each measurement was conducted at four flowrates that were averaged with five injections each. The rates at each flow rate were then averaged to obtain the final catalytic rates that are included in this report. SMSI coverage was calculated using the ratio of the catalytic rate when re-reduced at 300-550 °C (SMSI) and re-reduced at 200 °C (non-SMSI).

2.2.5 CO Infrared Spectroscopy

CO infrared spectroscopy was performed on a Thermo Nicolet iS50 instrument with a mercury cadmium telluride (MCT) detector to determine the binding modes of the control and SMSI catalysts. Each spectrum was recorded by collecting 32 scans from 4000 to 650 cm^{-1} at a resolution of 8 cm^{-1}. Spectra were collected until equilibrium had been achieved. This was done by scanning until there were no changes in spectra over time. The 0.1-1.0 wt% Ti containing catalysts were reduced in pure H_2 at 550 °C prior to analysis at 30 °C in pure CO. Ar was used to purge samples at 350 °C between gas treatments (pure Ar, 30 mL/min). Peaks were assigned for all catalysts as follows: atop bonding (2083 cm^{-1}), bridge bonding (1920-1950 cm^{-1}), and three-fold bonding (1840 cm^{-1}) which is consistent with past studies[31,34].

2.2.6 In situ X-ray Absorption Spectroscopy (XAS)

In situ XAS measurements were conducted at the 10-BM-B beamline at the Advanced Photon Source (APS) of Argonne National Lab at the Pd K edge (24.350 keV) to determine the Pd coordination environment and estimate particle sizes. The first set of measurements were conducting using catalysts that were pre-reduced from 250-550 °C. These catalysts were re-reduced at 200 °C for 30 minutes prior to scanning at room temperature in He. A second set of measurements were used to determine if particle sizes change after 350 °C oxidation and 200 °C re-reduction as well as how much Pd in the sample becomes oxidized after each stage of oxidation. The catalysts were scanned at room temperature after each of the following steps: reduced at 550 °C, oxidized at 30 °C, oxidized at 200/300/350 °C, and re-reduced at 200 °C. All scans were conducted at room temperature. For this set, the reduced catalyst scans were taken under flowing 5% H_2/He and the oxidized samples were scanned under flowing He. All samples were ground into a fine powder, pressed into a 6-shooter sample holder, and sealed in a sample cell with Kapton end caps. A gas purifier was connected to the He tank used for analysis to reduce the possibility of O_2 exposure upon cell cooling. Samples were analyzed with flowing He or flowing H_2. Measurements had a Pd foil and a third ion chamber that were used for energy calibrations. XAS data was fit using winXAS 3.1. Least-squares regression fits of the k^2-weighted Fourier transform data from 2.5 to 11.5 $Å^{-1}$ in k-space were used to obtain the extended x-ray absorption fine structure (EXAFS) coordination parameters. The first shell was used to fit all spectra. All samples were fit using experimental phases and amplitudes as well as theoretical scattering paths using FEFF. An S_o^2 value of 0.79 at a fixed coordination number of 12 for the Pd foil was used for all samples. All samples were then analyzed using theoretical scattering paths at controlled values of σ^2 for direct comparison.

2.2.7 Scanning Transmission Electron Microscopy (STEM)

Samples for scanning transmission electron microscopy (STEM) were prepared by drop-drying 3 μL of a 1 mg/mL supported catalyst suspension onto a Cu grid. High-angle annular dark-field scanning transmission electron microscopy (HAADF-STEM) were obtained on an FEI Talos F200X S/TEM with a 200 kV X-FEG field-emission source. 100 particles were imaged and the corresponding average particle size and particle size distribution were determined.

2.3 Results

2.3.1 Catalyst Synthesis

The 2Pd/SiO_2 (0 wt% Ti) catalysts were prepared by addition of Pd to SiO_2. At a pH of 11, the SiO_2 surface hydroxyls are deprotonated using NH_4OH. Addition of metal cations such as $Pd(NH_3)_4^{+2}$ leads to a strong Coulombic attraction and uniform surface coverage[35]. Calcination at moderate temperature leads to the formation of small metallic nanoparticles[36]. 2Pd-XTi/SiO_2 where X is the Ti wt% were prepared by addition of Ti to SiO_2 followed by Pd. All catalysts had 2 wt% Pd. The Ti was added via incipient wetness impregnation (IWI) of titanium(IV) bis(ammonium lactate) dihydroxide. The SMSI precursors were dried and calcined at 300 °C to remove the organic ligands. Pd was then added to all catalysts using IWI of tetraamminepalladium(II) nitrate. The catalysts were calcined at 450/600/700 °C and reduced at 250 °C.

2.3.2 Pd Nanoparticle Size Effects and Evidence for SMSI

2.3.2a Calcination Temperature

The effect of calcination temperature on Pd nanoparticle size was determined for catalysts with 0-1.0 wt% Ti loading. For this study, small sizes of ~2-4 nm are desirable in order to determine differences in CO uptake, propylene hydrogenation rates, and the CO IR spectra[37,38].

Pd CO chemisorption uptakes at 30 °C were used to determine relative changes in particle size with increasing calcination temperature. Propylene hydrogenation rates were also tested as a second method to support these results. The catalysts were tested after calcination at 450, 600, or 700 °C followed by reduction at 200 °C (Table 1). This low temperature reduction is necessary to avoid SMSI coverage which also reduces the CO uptake and propylene hydrogenation rate. All catalysts have similar CO uptakes and catalytic rates at a given calcination temperature indicating that TiO_2 had little effect on the Pd nanoparticle size. The CO uptakes were 0.32-0.39 with 450 °C calcination, 0.12-0.15 with 600 °C calcination, and 0.06-0.08 mol CO / mol Pd with 700 °C calcination. The propylene hydrogenation catalytic rates follow a similar trend where increasing

calcination temperature resulted in a drop in catalytic rate from 4.5-5.7 with 450 °C calcination, 2.5-4.2 with 600 °C calcination, and 1.2-1.7 mol C_3H_8*mol_{metal}^{-1}*s^{-1} with 700 °C calcination. Similar CO uptakes and rates for the Ti containing catalyst indicate that the Pd nanoparticle sizes increased similarly as calcination temperature was increased. Calcination at 450 °C gave the highest CO chemisorption and hydrogenation rates; therefore, this calcination temperature was used to synthesize the smallest Pd nanoparticle sizes in all catalysts.

Table 1. CO chemisorption and propylene hydrogenation results at 30 °C for catalysts calcined at different temperatures then reduced at 250 °C

Calcination Temperature (°C)	**Ti Loading (wt%)**	**CO Uptake (mol CO / mol Pd)**	**Catalytic Rate (mol C_3H_8*mol_{metal}^{-1}*s^{-1})**
450	0	0.32	5.7
	0.1	0.39	5.1
	0.5	0.35	4.5
	1.0	0.33	4.6
600	0	0.15	3.5
	0.1	0.12	4.2
	0.5	0.15	3.8
	1.0	0.12	2.5
700	0	0.07	1.7
	0.1	0.08	1.3
	0.5	0.08	1.7
	1.0	0.06	1.2

2.3.2b Reduction Temperature

CO uptakes at 30 °C were calculated for the 2Pd/SiO_2 (0 wt% Ti) catalyst calcined at 450 °C and reduced at 250-550 °C to determine how reduction temperature affects relative particle size. Increasing the reduction temperature decreased the CO uptake and the propylene hydrogenation rate (Table 2). The rate decreased from 5.7 to 2.6 mol C_3H_8*mol_{metal}^{-1}*s^{-1} and the CO uptake decreased from 0.32 to 0.12 mol CO / mol Pd when reduction temperature was increased from 250 to 550 °C. Since the CO:Pd ratio changes with Pd nanoparticle size, the particle size cannot be directly measured using chemisorption[39]. A more reliable method is needed that can also be used in the presence of SMSI. Thus, the effect of reduction temperature on particle size was tested using EXAFS of the Pd K edge to estimate Pd nanoparticle sizes from Pd-Pd first shell coordination[40].

Table 2. CO chemisorption and propylene hydrogenation rate results at 30 °C for the $2Pd/SiO_2$ (0 wt% Ti) catalyst calcined at 450 °C

Reduction Temperature (°C)	**CO Uptake (mol CO / mol Pd)**	**Catalytic Rate (mol C_3H_8*mol_{metal}^{-1}*s^{-1})**
250	0.32	5.7
400	0.25	5.5
500	0.12	3.2
550	0.12	2.6

In previous studies the Pt and Au M-M coordination number was shown to correlate with the nanoparticle size[40]. Thus, Pd K edge X-ray absorption fine structure (EXAFS) was used to determine the Pd-Pd coordination and the effect of increasing reduction temperature on particle size. Spectra were collected after reduction temperatures of 250/400/500/550 °C (Figure 1, Figure S1-S3). Coverage of the Pd nanoparticle surface by the SMSI oxide will not affect the estimated particle sizes.

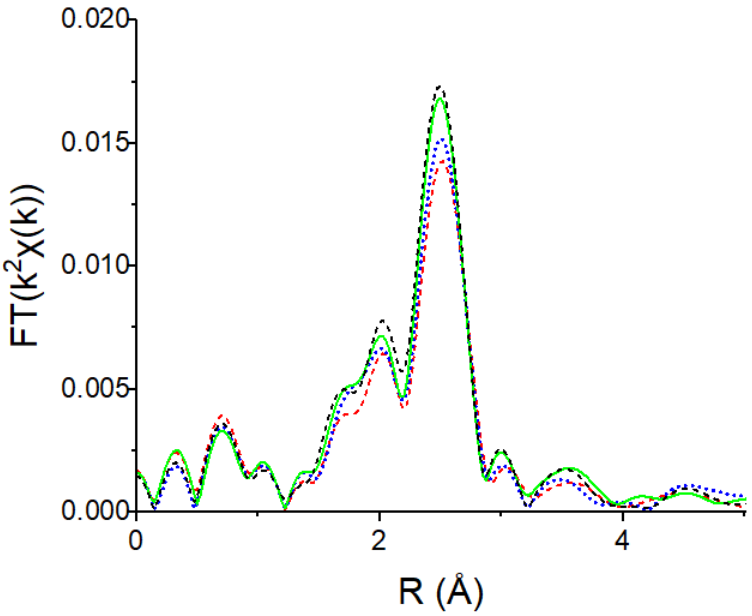

Figure 1. Pd K edge EXAFS spectra for $2Pd/SiO_2$ (0 wt% Ti) catalyst reduced at 250 (red, dash), 400 (blue, dot), 500 (green, solid), and 550 °C (black, dash)

There are 3 main peaks between 1.5 and 3.0 Å in R space of the k^2-weighted magnitude of the Fourier transforms which is typical for scattering of Pd nanoparticles[41,42] (Figure 1). A Pd-Pd

scattering path with a bulk bond distance of 2.75 Å was used to fit all samples. The phase and amplitude of the Pd foil (supported by theoretical scattering paths using FEFF) were used to determine the EXAFS fitting parameters (Table S1). The bond distances were all 0.01-0.03 Å smaller than the bulk Pd bond distance of 2.75 Å. This is typical of small metal nanoparticles which experience bond contraction due to a high fraction of low coordination surface atoms[43]. The Pd nanoparticle size increased with increasing reduction temperature for all catalysts (Figure 2, Table S1). The particle sizes were 1.0-1.5 nm when reduced at 250 °C and grew to ~2 nm when reduced at 550 °C. The Pd nanoparticles sintered significantly when reduced at 700 °C and the sizes were all similar regardless of Ti loading. Since SMSI Pd surface coverage will be determined after reduction at 550 °C due to small particle sizes, all catalysts were pre-reduced at 550 °C so that the size would not change after SMSI treatments.

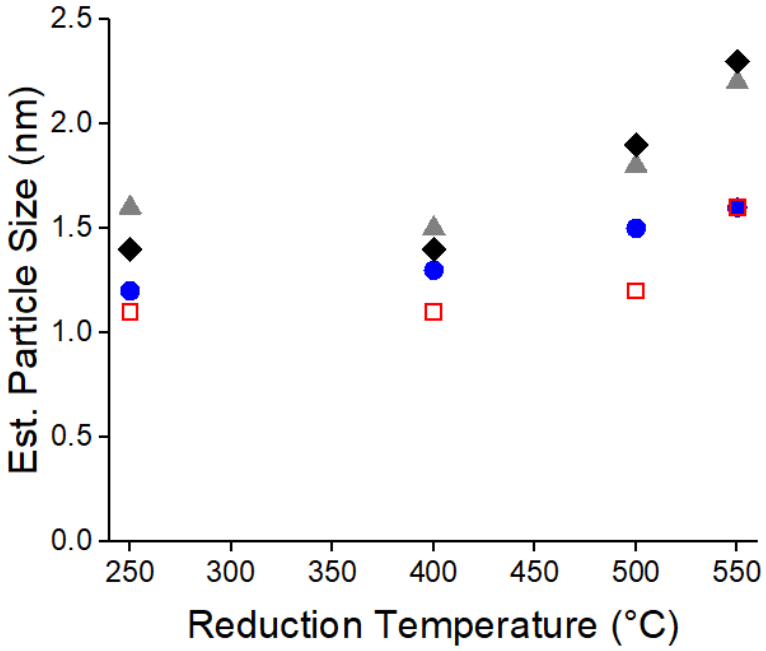

Figure 2. EXAFS particle sizes of 0 wt% Ti (blue, circle), 0.1 wt% Ti (red, square), 0.5 wt% Ti (grey, triangle), and 1.0 wt% Ti (black, diamond) containing catalysts

To confirm the Pd nanoparticle size, STEM images were obtained on the catalysts after reduction at 550 °C. A typical STEM image and particle size distribution are shown for 2Pd-0.5Ti/SiO_2 (Figure 3). The average Pd nanoparticle size for each catalyst is shown in Table 3 with

the sizes estimated by EXAFS. The STEM images and size distributions for the other catalysts are shown in Figure S4-S6.

Table 3. Particle sizes from EXAFS and STEM for catalysts reduced at 550 °C

Ti Loading (wt%)	EXAFS Est. Size (nm)	STEM Size (nm)
0	1.6	1.9 ± 0.4
0.1	1.6	1.9 ± 0.8
0.5	2.2	1.9 ± 0.6
1.0	2.3	1.9 ± 0.4

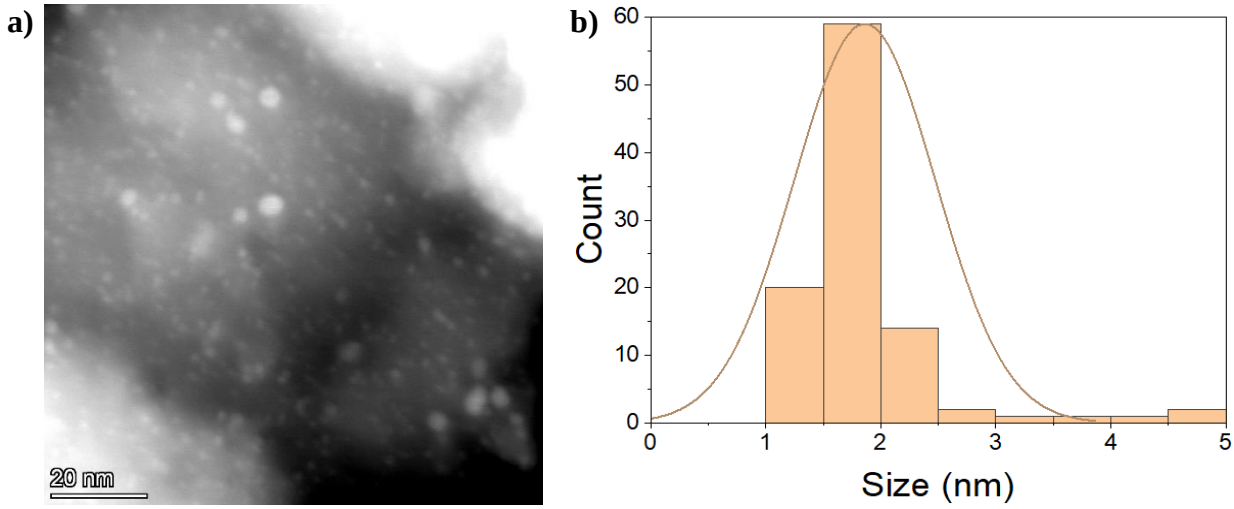

Figure 3. (a) STEM image and (b) particle size distribution of 2Pd-0.5Ti/SiO_2 catalyst after 550 °C reduction

2.3.2c Evidence for SMSI

Propylene hydrogenation was used to show that an SMSI effect occurs for the low content Ti containing catalysts (Figure 4, Table S2). The fraction of surface Pd atoms was determined from the EXAFS coordination numbers. Since the catalysts were reduced at 550 °C prior to reaction, a portion of the surface Pd atoms were covered which lowers the catalytic rate. The propylene hydrogenation rates and fraction of surface Pd atoms were used to calculate the apparent TORs, i.e., assuming that there is no coverage and all Pd surface atoms are active. The fraction of Pd surface atoms was calculated as 1/Size (sizes used from Table 3). The apparent TOR decreases from 4.0 to 0.9 s^{-1} as Ti loading is increased from 0 to 1.0 wt%. Propylene hydrogenation is a

known structure-insensitive reaction; therefore, the TOR should be constant regardless of changes to particle size[43]. The lower TORs for the Ti containing catalysts are a result of Pd surface coverage by $TiO_{(2-x)}$ SMSI species, i.e., not all surface Pd sites are exposed. At 1.0 wt% Ti, for example, there is a loss of ~80% of the expected rate, indicating that ~80% of the Pd nanoparticle surface is covered by $TiO_{(2-x)}$. The results also indicate that lower Pd surface coverages can be obtained by lowering the Ti loading (Table S3). For example, at 0.1% Ti, the surface coverage is approximately 40%. Lower loadings may provide even lower surface coverages.

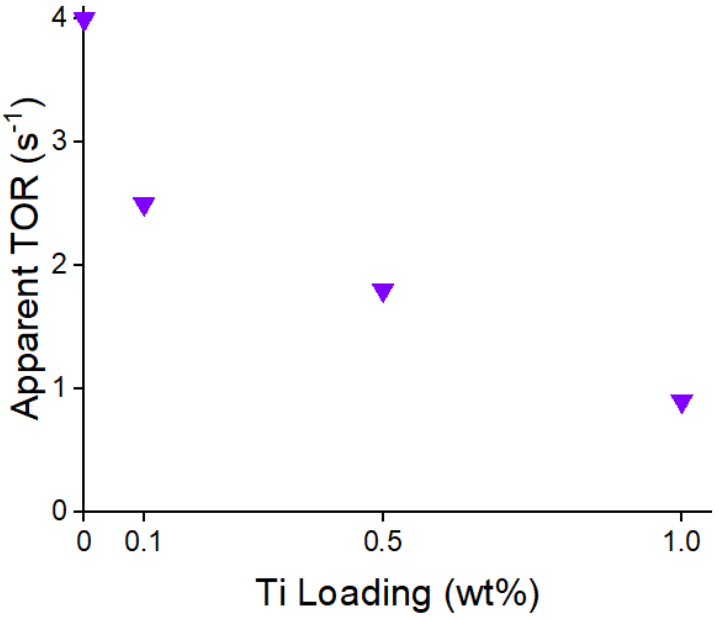

Figure 4. Estimated propylene hydrogenation TORs of all catalysts at 30 °C after 550 °C reduction

2.3.2d Infrared Spectra of Adsorbed CO on SMSI Pd Nanoparticles

The 0.1-1.0 wt% Ti containing catalysts calcined at 450 °C and reduced at 550 °C were analyzed using infrared (IR) spectroscopy of CO on Pd to determine which Pd surface sites are covered by the SMSI oxide. Face sites bond CO in a bridging or three-fold fashion while edge and corner sites bond CO linearly on a Pd nanoparticle[37]. The peaks at 2083 cm^{-1} corresponds to atop CO bonding on Pd sites. The peaks at 1920-1950 cm^{-1} and 1840 cm^{-1} correspond to bridge and three-fold bonding, respectively (Figure 5). The IR spectra of 2 nm Pd particles were previously

reported and showed high ratios of bridge and threefold (higher order) to linear bonding CO[37,38]. After reduction at 550 °C, the IR spectra of the 2Pd-XTi/SiO_2 SMSI catalysts show a significant fraction of linear bonded CO and a strong reduction in bridge and threefold bonded CO compared to the 0Ti-2Pd/SiO_2 catalyst. The ratio of higher order (bridging and three-fold) to linear CO bonding indicates that even at 0.1 wt% Ti few threefold face sites bond CO while corner and edge sites remain exposed. The ratio of higher order to linear bonding peak areas was 0.8-1.2 for all three SMSI catalysts (Table 4) which is much lower than 2.8 for Pd nanoparticles of the same size.

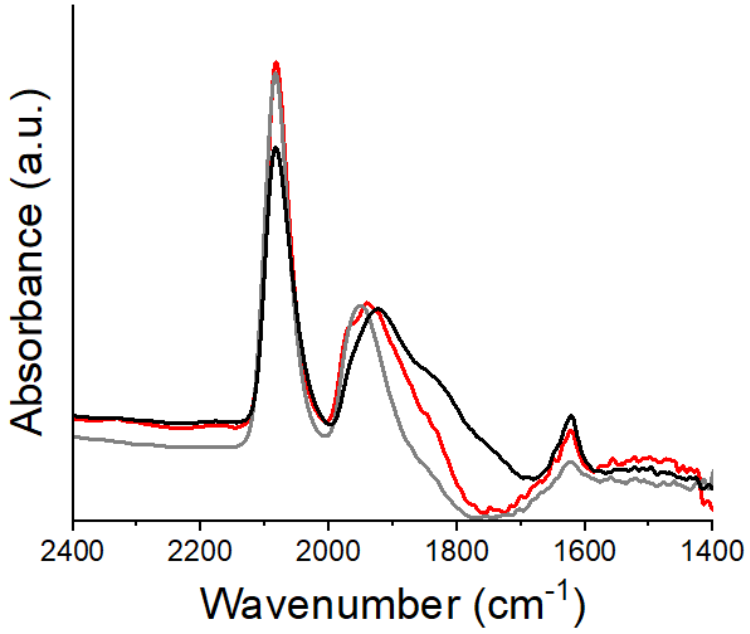

Figure 5. IR spectra of adsorbed CO at 30 °C on 0.1 (red), 0.5 (grey), and 1.0 (black) wt% Ti containing catalysts reduced at 550 °C

Table 4. CO IR peak area ratios at 30 °C for catalysts reduced at 550 °C

Ti Loading (wt%)	Higher Order to Linear Bonding Ratio
0	2.8
0.1	1.2
0.5	0.8
1	1.0

2.3.3 Reversibility of the SMSI State

2.3.3a Removal of the SMSI Overlayer

Tauster, et al. showed that the adsorption capacity of metallic nanoparticles covered by SMSI oxides can be restored by oxidation at 500 °C followed by low temperature reduction at 175 °C[2]. For the 2Pd-XTi/SiO_2 catalysts, oxidation at 350 °C and re-reduction at 200 °C fully removed the SMSI coverage and final Pd nanoparticle sizes were the same as when initially reduced at 550 °C (Table 5) based on XAS (Table S4) and STEM analysis (Figure S7-S9).

Table 5. Particle sizes for catalysts reduced at 550 °C, oxidized at 350 °C, and re-reduced at 200 °C

Ti Loading (wt%)	EXAFS Est. Size (nm)	STEM Size (nm)
0	1.5	-
0.1	1.9	2.0 ± 0.7
0.5	2.3	1.8 ± 0.6
1.0	2.3	2.0 ± 0.9

The propylene hydrogenation TORs of the catalysts reduced at 550 °C, oxidized at 350 °C and re-reduced at 200 °C are show in Table 6. The catalytic rates were all similar and the average TOR was 5.5 ± 1.3 s^{-1} was consistent with the literature for 1-3 nm Pd particles on alumina which had TORs of 4.4-12 s^{-1} [45].

Table 6. Propylene hydrogenation results at 30 °C for catalysts reduced at 550 °C, oxidized at 350 °C, and re-reduced at 200 °C

Ti Loading (wt%)	Rate (mol C_3H_8*mol_{metal}^{-1}*s^{-1})	Dispersion	TOR (s^{-1})
0	2.6	0.64	4.0
0.1	2.7	0.57	4.7
0.5	3.1	0.44	7.0
1	2.7	0.44	6.1

Since the nanoparticle size does not change after 350 °C oxidation and low temperature reduction, the fractional surface Pd nanoparticle coverage can be determine by the ratio of the propylene hydrogenation rate after high temperature reduction (SMSI covered Pd nanoparticles) divided by the rate after oxidation and re-reduction where the SMSI oxide over layer has been fully removed (Table S3). Based on the rates with and without SMSI coverage, the fractional Pd nanoparticle surface coverage is shown to increase with increasing Ti loading (Figure 6).

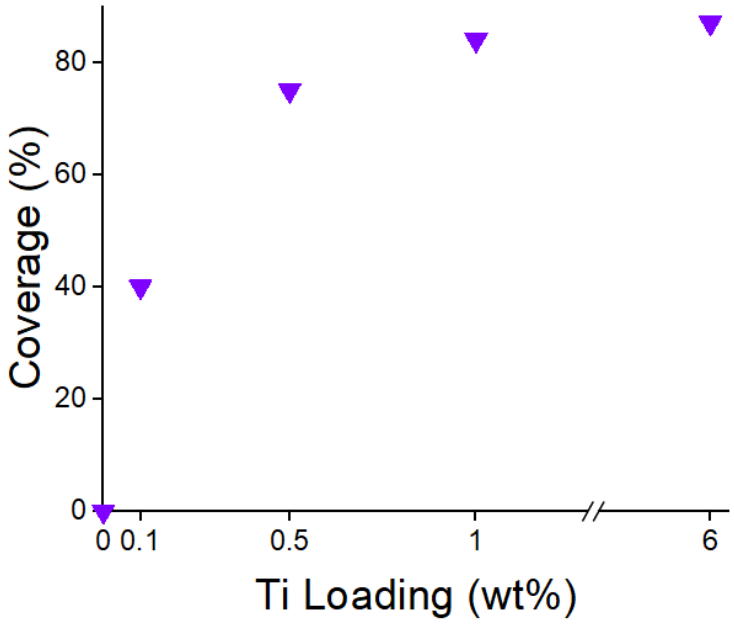

Figure 6. SMSI coverage for 0.1-6.0 wt% Ti catalysts reduced at 550 °C

2.3.3b Oxidation at Temperatures below 350 °C

While oxidation at 350 °C leads to a complete loss of the SMSI overlayer on the Pd nanoparticles, the catalysts were also oxidized at lower temperatures. All catalysts were analyzed using EXAFS to determine the fraction of Pd oxidized after 30 °C (Table 7). Partial SMSI coverage will result in incomplete surface oxidation. At 30 °C only exposed surface Pd is oxidized, and a new peak at 1.55 Å appears in the EXAFS due to PdO bond formation (Figure 7, Figure S10-12). In addition, there is a loss of metallic Pd-Pd scattering peaks.

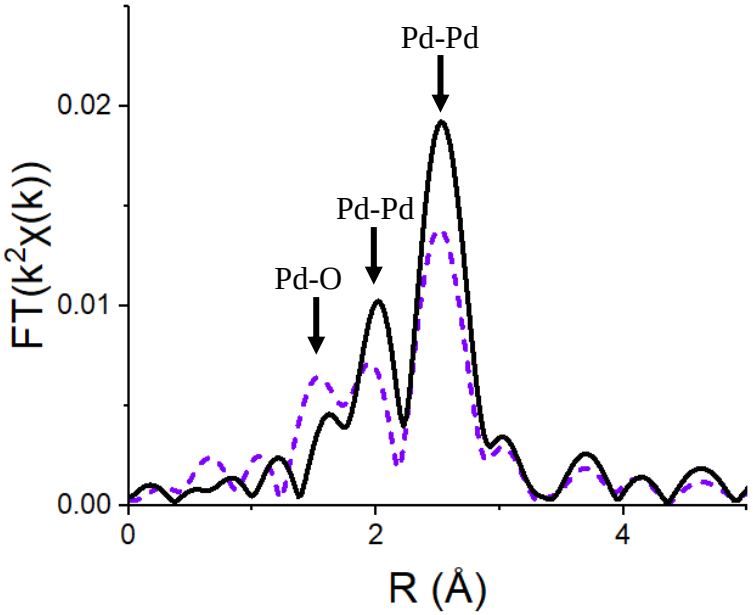

Figure 7. k^2-weighthed Fourier transform Pd K edge EXAFS spectra of the $2Pd/SiO_2$ (0 wt% Ti) catalyst reduced at 550 °C (black, solid) then oxidized at 30 °C (purple, dash)

Based on the nanoparticle size determined from EXAFS and STEM (Table 3) and EXAFS of the reduced Pd nanoparticles (Figure 1, Figure S1-S3), the fraction of surface Pd atoms in each catalyst was estimated. The fraction Pd oxidized in each catalyst was determine from Pd-O coordination numbers (CN) of the fits for 30 °C oxidized catalysts. For fully oxidized Pd there are 4 Pd-O bonds, thus the fraction of oxidized Pd in any catalyst is given by the Pd-O CN/4. The surface fraction oxidized Pd decreases from 0.95 for $2Pd/SiO_2$ to as low as 0.28 at 1.0 wt% Ti (Table 7). This indicates that the SMSI overlayer prevents oxidation of the surface Pd atoms that it covers. Increasing the Ti loading from 0.1 to 1.0 wt% increased the fraction of the nanoparticle surface that was covered.

Table 7. Fraction of Pd nanoparticle surface covered by $TiO_{(2-x)}$ with increasing Ti loading after 550 °C reduction and 30 °C oxidation

Ti Loading (wt%)	Surface Fraction Pd Oxidized	Fraction of Surface Pd Covered by SMSI
0	0.95	-
0.1	0.44	0.54
0.5	0.33	0.66
1.0	0.28	0.72

The rate of propylene hydrogenation of SMSI covered Pd nanoparticles initially reduced at 550 °C was determined after oxidation with increasing temperature and re-reduction at 200 °C. For the 2Pd-0.5Ti/SiO_2 catalyst, the rate increases with increasing oxidation temperature suggesting that increasing oxidation temperatures partially removes the SMSI overlayer (Figure 8a, Table S5). Above 350 °C, the catalytic rate remained constant at ~3.1 mol C_3H_8*mol_{metal}^{-1}*s^{-1} corresponding to a TOR of 6.8 s^{-1} which is consistent with past studies of ~2 nm Pd particles[44] suggesting there is little to no SMSI coverage remaining.

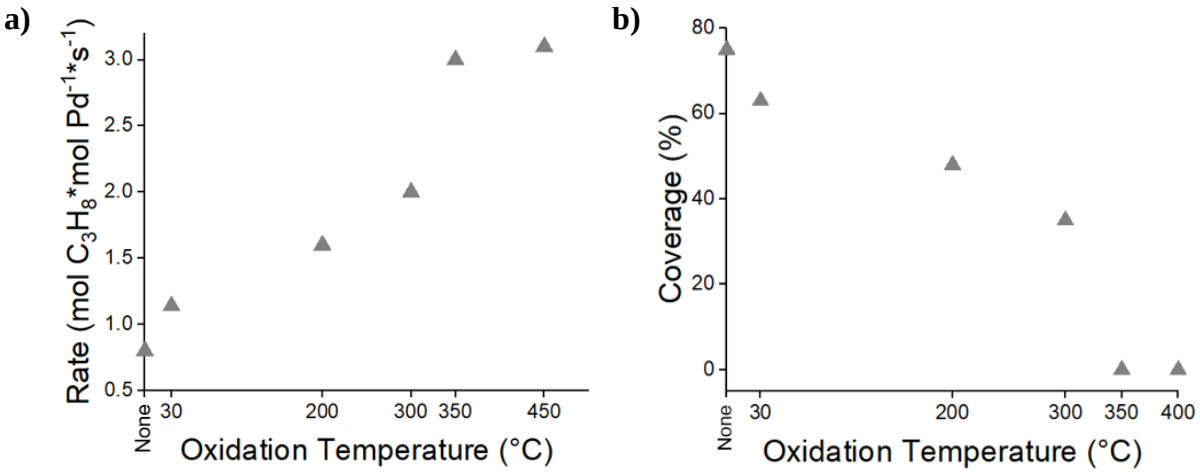

Figure 8. (a) Propylene hydrogenation rate and (b) fractional SMSI coverage of 2Pd-0.5Ti/SiO_2 catalyst reduced at 550 °C, oxidized, and re-reduced at 200 °C

The remaining coverage can be measured for the samples when oxidized below 350 °C, i.e., the rates after oxidation at low temperature and re-reduction at 200 °C divided by the rate after complete removal with 350 °C oxidation and 200 °C re-reduction (Figure 8b, Table S5). For 2Pd-0.5Ti/SiO_2, the Pd nanoparticle surface coverage is 75% after 550 °C reduction and no oxidation. Using an oxidation step with increasing temperature and re-reduction at 200 °C results in a lower SMSI coverage. Thus, the oxidation temperature can be used to control the SMSI coverage, at least for low temperature reactions.

The fraction of total Pd that was oxidized with increasing temperature was determined by EXAFS. As the oxidation temperature increased the Pd-O coordination number increased (Table S6). Since fully oxidized PdO has a coordination number of 4, the fraction of oxidized Pd with

increasing temperature was estimated by determining the catalysts Pd-O CN/4. Increasing the oxidation temperature increases the fraction of oxidized Pd in all catalysts (Figure 9). At 30° C exposed surface Pd atoms are oxidized. At higher oxidation temperatures Pd that is covered by the SMSI oxide is oxidized. At 350 °C, where there is little remaining SMSI coverage, there is also little metallic Pd. The EXAFS suggests that removal of the SMSI overlayer requires the oxidation of the metallic Pd covered by the SMSI oxide. For high coverages of the SMSI oxide this requires nearly complete oxidation of the metallic nanoparticle.

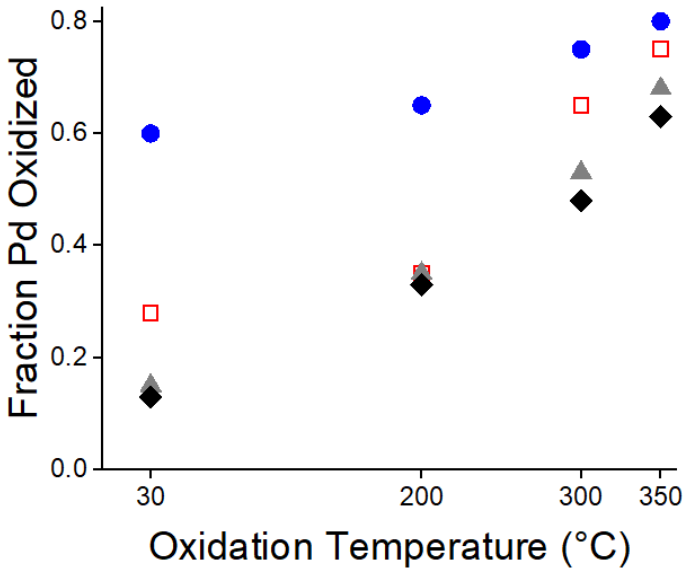

Figure 9. Fraction Pd oxidized for 0 wt% Ti (blue, circle), 0.1 wt% Ti (red, square), 0.5 wt% Ti (grey, triangle), and 1.0 wt% Ti (black, diamond) containing catalysts initially reduced at 550 °C

2.3.4 Controlling Partial SMSI Coverage by Increasing the Re-reduction Temperature

As shown above, the fraction of SMSI coverage can be determined from the propylene hydrogenation rate at 30 °C with and without SMSI coverage. As demonstrated in Figure 6, the Pd nanoparticle coverage can be controlled by the Ti loading where coverages of less than ~50% would require ~0.2 wt% Ti or less. Additionally, the SMSI coverage for low temperature reactions can be controlled by oxidation of the SMSI catalyst at temperatures below 350 °C. While the SMSI overlayer can be removed at 350 °C, partial removal occurs at lower oxidation temperatures (Figure 8b).

The 2Pd-XTi/SiO_2 (0.1–1.0 wt% Ti) SMSI catalysts were reduced at 550 °C, oxidized at 350 °C, and re-reduced at 200 °C through five oxidation and re-reduction cycles and the CO chemisorption uptake was measured to confirm that there were no changes in particle size after these treatments. The initial and final CO chemisorption values were identical (Table 8) indicating no changes in nanoparticle size for oxidation and reduction temperatures below 350 °C and 550 °C, respectively.

Table 8. CO uptake for 2Pd-XTi/SiO_2 catalysts reduced at 550 °C, oxidized at 350 °C, and re-reduced at 200 °C after multiple oxidation and re-reduction cycles

Ti Loading (wt%)	**200 °C Re-Reduction Measurement**	**CO Uptake (mol CO / mol Pd)**
0.1	Initial	0.29
	Final	0.28
0.5	Initial	0.26
	Final	0.28
1.0	Initial	0.21
	Final	0.22

The 2Pd-XTi/SiO_2 catalysts were reduced at 550 °C and oxidized at 350 °C to remove the SMSI overlayer. Each catalyst was subsequently re-reduced at increasing temperature from 200-550 °C. The propylene hydrogenation rate (measured at 30 °C) for each re-reduction temperature was divided by the rate of the catalyst re-reduced at 200 °C to determine the fraction of SMSI surface coverage (Figure 10, Table S7). For each Ti loading, the SMSI coverage increased with increasing reduction temperature. In addition, lower Ti loadings resulted in lower coverages at every reduction temperature. Decreasing the re-reduction temperature resulted in lower levels of coverage from ~10% after 300 °C re-reduction to ~35% after 500 °C re-reduction for 0.1 wt% Ti. For 1 wt% Ti, 84% of the catalytic surface was covered after 550 °C reduction. Intermediate coverages of 0-75% were achieved with 200-400 °C re-reduction temperatures. These differences in coverage indicate that re-reduction temperature is also an effective method to vary particle coverage as long as the reaction temperature is below the re-reduction temperature.

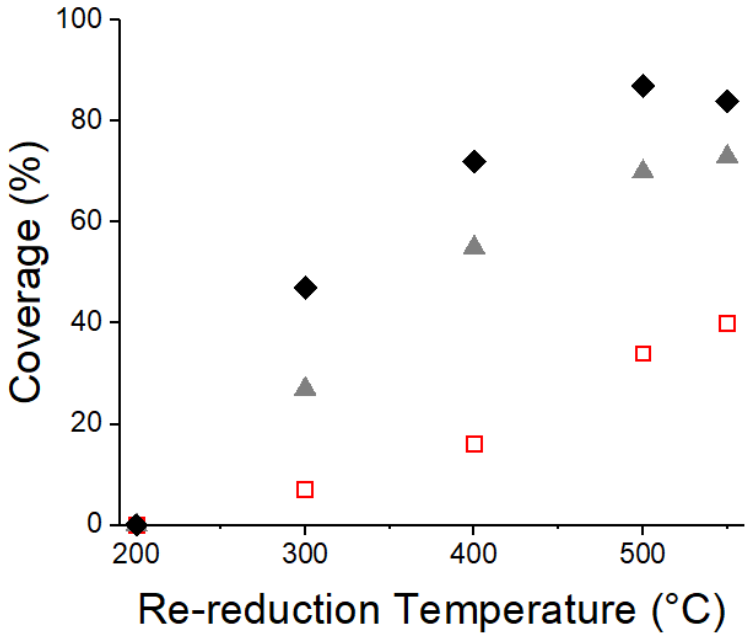

Figure 10. SMSI coverage for 0.1 wt% Ti (red, square), 0.5 wt% Ti (grey, triangle), and 1.0 wt% Ti (black, diamond) containing catalysts at varied re-reduction temperatures

2.4 Discussion

2.4.1 Evidence for SMSI and Conditions for Reversibility

SMSI has been widely studied for metallic nanoparticles on oxide supports such as TiO_2[10], CeO_2[12,13], Nb_2O_5[16], ZnO[18,19], and on SiO_2 and supported SMSI oxides[3,5,16]. For the latter, the weight loadings of SMSI oxide are typically greater than 1.0 wt%. For both types, the NP surface is highly covered, often greater than 70%. In this study, we present three methods for controlling the SMSI coverage from 10-85%. To determine the Pd surface coverage by the SMSI oxide, one needs to compare the rate of propylene hydrogenation, a structure insensitive reaction in which the rate of every surface Pd is identical, with and without the SMSI overlayer. As shown by Tauster, et al. the SMSI oxide can be removed by oxidation at high temperature[2]. For these 2Pd-XTi/SiO_2 catalysts, oxidation at temperatures of 350 °C led to nearly complete oxidation of the metallic Pd nanoparticles and reversal of the SMSI coverage. Re-reduction at 200 °C restored the Pd nanoparticles without formation of the SMSI overlayer. As shown by STEM and EXAFS, these treatments did not alter the Pd nanoparticle size. Comparison of the propylene hydrogenation rates for the SMSI and SMSI-free states allows for determination of the Pd surface coverage as shown

in Figure 11. Steps 1 (calcination at 450 °C) and 2 (reduction at 550 °C) give small metallic nanoparticles with the maximum SMSI coverage. Step 3 (oxidation at 350 °C) gives PdO and removes the SMSI overlayer. Step 4 (re-reduction at 200 °C) gives Pd nanoparticles of the same size as in Step 2 but without the SMSI surface coverage. Comparison of the propylene hydrogenation rate after Step 2 and 4 gives the fractional SMSI surface coverage.

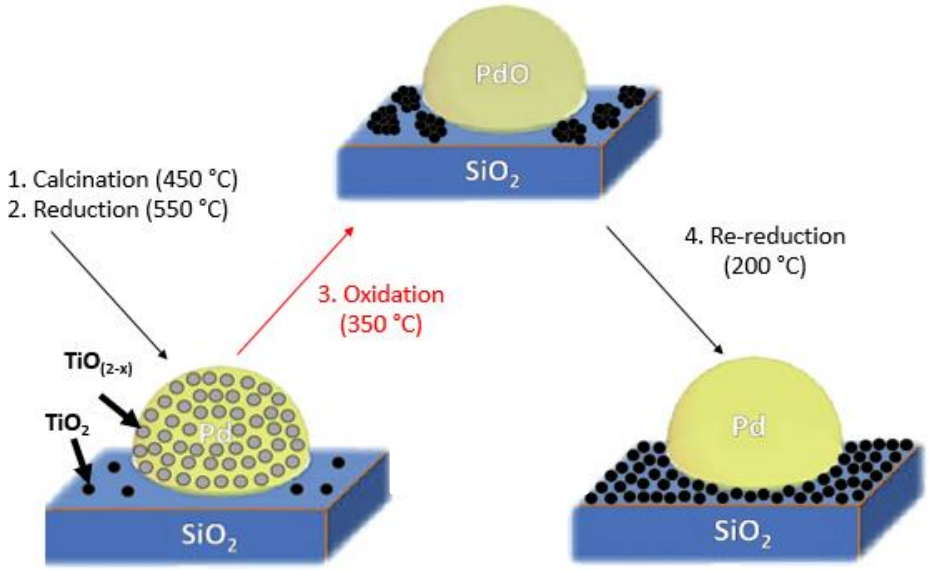

Figure 11. Determination of the fractional SMSI oxide coverage

2.4.2 Partial Coverage of Pd Nanoparticles by $TiO_{(2-x)}$ SMSI Oxides

The first method to control the Pd surface coverage is to control the Ti loading and reduce the catalyst at high temperature (550 °C) to give the maximum coverage for that loading. For example, with 0.1 wt% Ti, the Pd nanoparticle surface coverage is ~40%. While lower SMSI surface coverages were not investigated in this study, Ti loadings of less than 0.1 wt% would be expected to give even lower coverages. With 0.5 wt% Ti the surface coverage is ~75%. At coverages of 1% or higher, the Pd surface coverage is nearly constant at ~85% as seen in a previous study[3].

It is surprising that 0.1 wt% Ti can lead to a loss of 40% of the Pd surface sites. For example, on a 1.6 nm sized Pd nanoparticle in 2% Pd/SiO_2 the dispersion is 0.62. The ratio of surface Pd to

Ti is approximately 6. In addition, not all of the $TiO_{(2-x)}$ would be expected to be near the Pd nanoparticles. In order for 0.1% Ti to reduce the catalytic rate by 40%, a high fraction of the $TiO_{(2-x)}$ would have to be covering the Pd nanoparticle surface and each $TiO_{(2-x)}$ species would have to be covering more than one active site. Based on the IR spectra, the SMSI oxide selectively covers threefold Pd surface sites. Therefore, the SMSI oxide likely blocks more than one active site per Ti. If each SMSI oxide were to block three catalytic sites, this would require ~0.07% Ti to give a surface coverage of 40%. This also assumes that all of the Ti added to the catalyst is on the SMSI oxide with little remaining on the support. This suggests that at low loadings much of the $TiO_{(2-x)}$ is near or covering the Pd nanoparticles. High resolution electron microscopy techniques such as EDX may prove useful in determining this as well as the local structure of the partial SMSI overlayer.

The second method to control the Pd nanoparticle coverage by the SMSI oxide is to re-reduce the SMSI-free catalyst (Step 4 in Figure 10) at increasing temperatures. While there is little SMSI coverage upon reduction at 200 °C, the SMSI coverage increases at temperatures from 300-550 °C as seen in Figure 10. Re-reduction combined with low Ti loading gives surface coverages as low as 10%. The limitation of this method is that, to maintain the low surface coverage, the reaction temperature must be lower than the re-reduction temperature. However, by reducing the Ti loading, one can get the same surface coverage at a higher temperature. For example, with 0.1 wt% Ti a surface coverage of 30% is achieved using re-reduction at ~500 °C while for 0.5 wt% Ti the same surface coverage is possible using re-reduction at 300 °C (Figure 10).

The third method for controlling the SMSI coverage is by using low temperature oxidation of the SMSI catalyst (Figure 7). Room temperature air exposure of the SMSI covered Pd nanoparticle resulted in oxidation of the exposed metallic Pd atoms. Room temperature air is well known to oxidize metallic surface atoms in noble metal catalysts and is the basis for the oxidation-reduction chemisorption method. Re-reduction of the oxidized surface atoms does not lead to any significant changes in the fraction of metallic surface Pd, the fraction of SMSI coverage, or nanoparticle size. Thus, the SMSI oxide is impermeable to O_2 and the metallic Pd atoms under the SMSI oxide are not oxidized. Increasing the oxidation temperature, however, does oxidize a portion of the metallic Pd covered by $TiO_{(2-x)}$. Re-reduction at 200 °C gives nanoparticles of the

same size but with a higher fraction of exposed Pd. The fraction of exposed metallic Pd increases with increasing oxidation temperature until 350 °C where the SMSI oxide no longer covers the metallic Pd nanoparticles and the surface is fully metallic after 200 °C re-reduction. Oxidation at 350 °C leads to nearly complete oxidation of the metallic Pd nanoparticles. Thus, to remove the SMSI overlayer, one needs to oxidize the metallic atoms at the Pd-SMSI oxide interface. Since the SMSI oxide is impermeable to O_2 and the fraction of oxidized Pd increases with increasing temperature, it is likely that oxidation of the SMSI covered Pd occurs at the edge of the SMSI oxide. As the temperature increases, sub-surface Pd oxidizes until the SMSI surface covered Pd is oxidized and the SMSI-Pd interface is fully removed. Removal of the SMSI oxide requires oxidation of the covered Pd atoms rather than migration of the SMSI oxide away from the Pd nanoparticle resulting surface oxidation and complete removal of the overlayer.

2.4.3 Controlling Partial Coverage for Improved SMSI Catalysts

The presence of the SMSI oxide has been shown to be beneficial for several catalytic reactions[3-9]; however, the high surface coverage of active sites leads to low rates. SMSI catalysts most often improve selectivity by suppressing hydrogenolysis reactions. The desired reaction rate, however, is also greatly reduced. Thus, the SMSI catalyst has improved selectivity but at a low rate. The latter is fractional compared to the rate of the SMSI-free catalyst.

For example, dehydrogenation of propane on ~2 nm Pt nanoparticles supported on SiO_2 had a 60% propylene selectivity and 40% hydrogenolysis selectivity to methane and ethane at 30% conversion[2]. Addition of SMSI oxides, for example Pt-Ti/SiO_2 and Pt-Nb/SiO_2 catalysts with 3% Ti and 4% Nb, suppressed hydrogenolysis giving propylene selectivities above 95%. As observed for these catalysts, the SMSI oxides resulted in the loss of over 80% of the active sites.

Similarly, Yang, et al. prepared Ni-Mo/SiO_2 catalysts for m-cresol hydrodeoxygenation which is a biomass model compound[46]. Under reaction conditions the Ni is reduced to Ni nanoparticles which are known for their high hydrogenolysis selectivity. The Mo:Ni molar ratios were varied and the catalytic performance was determined. At low Mo:Ni ratios and at high reaction temperature there is a high selectivity for hydrogenolysis and formation of CH_4. At a Mo:Ni ratio near one hydrogenolysis is suppressed and hydrodeoxygenation leads to high

selectivity to toluene. Further increases in the Mo:Ni ratio maintains the high selectivity but reduces the rates suggesting extensive coverage of active sites. Thus, controlling the active site coverage can lead to improved selectivity and higher rates.

The goal of this study was to determine if one can control the SMSI active site coverage to lower levels than is generally obtained with the hope of improving the rate while maintaining high selectivity. We demonstrate that the coverage can be controlled resulting in catalysts with higher activity; however, much lower SMSI loadings are required than what have typically been used. The effect on selectivity will depend on the specific reaction; however, based on the IR spectra, it appears that the SMSI oxide at low coverages occupies threefold surface sites which are known to be active sites for hydrogenolysis, for example. This study provides another option for synthesis of catalysts with improved performance.

2.5 Conclusions

~2 nm sized 2 wt% Pd/SiO_2 catalysts with 0-1.0 wt% Ti were synthesized using calcination at 450 °C and reduction at 550 °C. Calcination and reduction at higher temperatures led to slightly larger nanoparticles. Catalysts containing 0.1-1.0 wt% $TiO_{(2-x)}$ had reduced CO chemisorption capacities and lower propylene hydrogenation rates compare to Pd/SiO_2 of the same size suggesting coverage of the Pd nanoparticles by the $TiO_{(2-x)}$ SMSI oxide. The Pd nanoparticle surface coverage increased with increasing Ti loading. Oxidation at 350 °C followed by reduction at 200 °C removed the SMSI overlayer and did not change the Pd nanoparticle size. Thus, the fractional coverage of the Pd nanoparticles was determined from the ratio of the propylene hydrogenation rate with SMSI coverage divided by that without SMSI coverage. For Ti loadings from 0.1 to 1.0 wt%, the SMSI coverage increased from about 40-85%. Surface coverage of 40% suggests that most of the Ti is covering the Pd nanoparticles and that each SMSI oxide species leads to the loss of more than one active site. Consistent with this conclusion, the IR spectra of adsorbed CO show that the SMSI oxides are selectively blocking Pd threefold sites.

Following oxidation at 350 °C, partial SMSI coverage can also be controlled by re-reducing at temperatures from 300-500 °C. The low temperature re-reduction can be combined with low Ti

loadings to give surface coverages as low as 10%. To retain low surface coverage the reaction temperature must be lower than the re-reduction temperature; however, by reducing the Ti loading, one can get the same surface coverage at a higher temperature. Finally, the SMSI surface coverage can be controlled by oxidation at temperatures below 350 °C followed by re-reduction at 200 °C. With increasing oxidation temperature, EXAFS shows that there is an increasing fraction of oxidized Pd. At 350 °C, where the SMSI oxide is fully removed, the metallic Pd nanoparticles are nearly fully oxidized. These results suggest that oxidation of the metallic Pd is required to remove the SMSI oxide overlayer. By controlling the SMSI oxide loading to levels of less than 1 wt%, it is suggested that catalysts with high selectivity and improved activity are possible.

2.6 References

[1] Breckner, C. J.; Zhu, K.; Wang, M.; Zhang, G.; Li, C. W.; Miller, J. T.; "Controlled site coverage of strong metal-support interaction (SMSI) on Pd NP catalysts," *Catal. Sci. Technol.*, 2023, **13**, 157-169.

[2] Tauster, S. J.; Fung, S. C.; Garten, R. L., "Strong Metal-Support Interactions. Group 8 Noble Metals Supported on TiO_2", *J. Am. Chem. Soc.*, 1978, **100**, 170-175.

[3] Zhu Chen, J.; Gao, J.; Probus, P. R.; Liu, W.; Wu, X.; Wegener, E. C.; Kropf, A. J.; Zemlyanov, D.; Zhang, G.; Yang, X.; Miller, J. T., "The effect of strong metal-support interaction (SMSI) on Pt-Ti/SiO_2 and Pt-Nb/SiO_2 catalysts for propane dehydrogenation", *Catal. Sci. Technol.*, 2020, **10**, 5973-5982.

[4] Kim, W. J.; Kang, J. H.; Ahn, I. Y.; Moon, S. H., "Deactivation behavior of a TiO_2-added Pd catalyst in acetylene hydrogenation", *J. Catal.*, 2004, **226**, 226-229.

[5] Kang, J. H.; Shin, E. W.; Kim, W. J.; Park, J. D.; Moon, S. H., "Selective hydrogenation of acetylene on Pd/SiO_2 catalysts promoted with Ti, Nb and Ce oxides", *Catal. Today*, 2000, **63**, 183-188.

[6] Kang, J. H.; Shin, E. W.; Kim, W. J.; Park, J. D.; Moon, S. H., "Selective Hydrogenation of Acetylene on TiO_2-Added Pd Catalysts", *J. Catal.*, 2002, **208**, 310-320.

[7] Jenness, G. R.; Schmidt, J. R., "Unraveling the Role of Metal-Support Interactions in Heterogeneous Catalysis: Oxygenate Selectivity on Fischer-Tropsch Synthesis", *ACS Catal.*, 2013, **3**, 2881-2890.

[8] Rodriguez, J. A.; Liu, P.; Hrbek, J.; Evans, J.; Pérez, M., "Water Gas Shift Reaction on Cu and Au Nanoparticles Supported on CeO_2(111) and ZnO(000): Intrinsic Activity and Importance of Support Interactions", *Angew. Chem. Int. Ed.*, 2007, **46**, 1329-1332.

[9] Kumar, A.; Ramani, V., "Strong Metal-Support Interactions Enhance the Activity and Durability of Platinum Supported on Tantalum-Modified Titanium Dioxide Electrocatalysts", *ACS Catal.*, 2014, **4**, 1516-1525.

[10] Tauster, S. J.; Fung, S. C.; Baker, R. T. K.; Horsley, J. A., "Strong interactions in supported-metal catalysts", *Science*, 1981, **211**, 1121-1125.

[11] Dulub, O.; Hebenstreit, W.; Diebold, U., "Imaging Cluster Surfaces with Atomic Resolution: The Strong Metal-Support Interaction State of Pt Supported on TiO_2(110)", *Phys. Rev. Lett.*, 2000, **84**, 3646-3649.

[12] Datye, A. K.; Kalakkad, D. S.; Yao, M. H.; Smith, D. J., "Comparison of metal-support interactions in Pt/TiO_2 and Pt/CeO_2", *J. Catal.*, 1995, **155**, 149-153.

[13] Campbell, C. T., "Electronic perturbations", *Nat. Chem.*, 2012, **4**, 597-598.

[14] Willinger, M. C.; Zhang, W.; Bondarchuk, O.; Shaikhutdinov, S.; Freund, H. J.; Schlögl, R., "A Case of Strong Metal-Support Interactions: Combined Advanced Microscopy and Model Systems to Elucidate the Atomic Structure of Interfaces", *Angew. Chem. Int. Ed.*, 2014, **53**, 5998-6001.

[15] Kast, P.; Friedrich, M.; Teschner, D.; Girgdies, F.; Lunkenbein, T.; d'Alnoncourt, R. N.; Behrens, M.; Schlögl, R., "CO oxidation as a test reaction for strong metal-support interaction in nanostructured Pd/FeO_x powder catalysts", *Appl. Catal. A-Gen.*, 2015, **502**, 8-17.

[16] Ahn, I. Y.; Kim, W. J.; Moon, S. H., "Performance of La_2O_3- or Nb_2O_5-added Pd/SiO_2 catalysts in acetylene hydrogenation", *Appl. Catal. A-Gen.*, 2006, **308**, 75-81.

[17] Mo, S.; Zhang, Q.; Zhang, M.; Zhanq, Q.; Li, J.; Fu, M.; Wu, J.; Chen, P.; Ye, D., "Elucidating the special role of strong metal-support interactions in Pt/MnO_2 catalysts for total toluene oxidation", *Nanoscale Horiz.*, 2019, **4**, 1425-1433.

[18] Liu, X.; Liu, M.H.; Luo, Y.C.; Mou, C.Y.; Lin, S.D.; Cheng, H.; Chen, J.M.; Lee, J.F.; Lin, T.S., "Strong Metal-Support Interactions between Gold Nanoparticles and ZnO Nanorods in CO Oxidation", *J. Am. Chem. Soc.*, 2012, **134**, 10251-10258.

[19] Gao, J.; Sawant, K. J.; Miller, J. T.; Zeng, Z., Zemlyanov, D.; Greeley, J. P., "Structural and Chemical Transformations of Zinc Oxide Ultrathin Films on Pd(111) Surfaces.", *ACS Appl. Mater. Interfaces*, 2021, **13**, 35113-35123.

[20] Tang, H.; Wei, J.; Liu, F.; Qiao, B.; Pan, X.; Li, L.; Liu, J.; Wang, J.; Zhang, T., "Strong Metal-Support Interactins between Gold Nanoparticles and Nonoxides", *J. Am. Chem. Soc.*, 2016, **138**, 56-59.

[21] Liu, S.; Xu, W.; Niu, Y.; Zhang, B.; Zheng, L.; Liu, W.; Li, L.; Wang, J., "Ultrastable Au nanoparticles on titania through an encapsulation strategy under oxidative atmosphere", *Nat. Comm.*, 2019, **10**, 5790.

[22] Dong, J.; Fu, Q.; Li, H.; Xiao, J.; Yang, B.; Zhang, B.; Bai, Y.; Song, T.; Zhang, R.; Gao, L.; Cai, J.;Zhang, H.; Liu, Z.; Bao, X., "Reaction-Induced Strong Metal-Support Interactions between Metals and Inert Boron Nitride Nanosheets", *J. Am. Chem. Soc.*, 2020, **142**, 17167-17174.

[23] Farmer, J. A.; Campbell, C. T., "Ceria Maintains Smaller Metal Catalyst Particles by Strong Metal-Support Bonding", *Science*, 2010, **329**, 933-936.

[24] Matsubu, J. C.; Zhang, S.; DeRita, L.; Marinkociv, N. S.; Chen, J. G.; Grahaw, G. W.; Pan, X.; Christopher, P., "Adsorbate-mediated strong metal-support interactions in oxide-supported Rh catalysts", *Nat. Chem.*, 2017, **9**, 120-127.

[25] Lee, J.; Burt, S. P.; Carrero, C. A.; Alba-Rubio, A. C.; Ro, I.; O'Neil, B. J.; Jim, H. J.; Jackson, D. H.K.; Kuech, T. F.; Hermans, I.; Dumesic, J. A.; Huber, G. W., "Stabilizing cobalt catalysts for aqueous-phase reactions by strong metal-support interaction", *J. Catal.*, 2015, **330**, 19-27.

[26] Alexeev, O. S.; Chin, S. Y.; Engelhard, M. H.; Ortiz-Soto, L.; Amiridis, M. D., "Effects of Reduction Temperature and Metal-Support Interactions on the Catalytic Activity of Pt/γ-Al_2O_3 and Pt/TiO_2 for the Oxidation of CO in the Presence and Absence of H_2", *J. Phys. Chem. B*, 2005, **109**, 23430-23443.

[27] Han, B.; Guo, Y.; Huang, Y.; Xi, W.; Xu, J.; Luo, J.; Qi, H.; Ren, Y.; Liu, X.; Qiao, B.; Zhang, T., "Strong Metal-Support Interactions between Pt Single Atoms and TiO_2", *Angew. Chem. Int. Ed.*, 2020, **59**, 11824-11829.

[28] Chu, M.; Pan, Q.; Bian, W.; Liu, Y.; Cao, M.; Zhang, C.; Lin, H.; Zhang, Q.; Xu, Y., "Strong metal-support interaction between palladium and gallium oxide within monodisperse nanoparticles: self-supported catalysts for propyne semi-hydrogenation", *J. Catal.*, 2021, **395**, 36-45.

[29] Liu, X.; Liu, M.H.; Luo, Y.C.; Mou, C.Y.; Lin, S.D.; Cheng, H.; Chen, J.M.; Lee, J.F.; Lin, T.S., "Strong Metal-Support Interactions between Gold Nanoparticles and ZnO Nanorods in CO Oxidation", *J. Am. Chem. Soc.*, 2012, **134**, 10251-10258.

[30] Zhang, S.; Plessow, P. N.; Willis, J. J.; Dai, S.; Xu, M.; Graham, G. W.; Cargneloo, M.; Abild-Pedersen, F.; Pan, X., "Dynamical Observation and Detailed Description of Catalysts under Strong Metal-Support Interaction", *Nano Lett.*, 2016, **16**, 4528-4534.

[31] Polo-Garzon, F.; Blum, T.; Bao, Z.; Wang, K.; Fung, V.; Huang, Z.; Bickel, E. E.; Jiang, D.; Chi, M.; Wu, Z., "*In* Situ Strong Metal-Support Interaction (SMSI) Affects Catalytic Alcohol Conversion", *ACS Catal.*, 2021, **11**, 1938-1945.

[32] Armbrüster, M., Schlögl, R.; Grin, Y., "Intermetallic compounds in heterogeneous catalysis - a quickly developing field", *Sci. Tecnhol. Adv. Mater.*, 2014, **15**, 034803.

[33] Lee, J.; Burt, S. P.; Carrero, C. A.; Alba-Rubio, A. C.; Ro, I.; O'Neil, B. J.; Jim, H. J.; Jackson, D. H.K.; Kuech, T. F.; Hermans, I.; Dumesic, J. A.; Huber, G. W., "Stabilizing cobalt catalysts for aqueous-phase reactions by strong metal-support interaction", *J. Catal.*, 2015, **330**, 19-27.

[34] Childers, D. J.; Schweitzer, N. M.; Shahari, S. M.; Rioux, R. M.; Miller, J. T.; Meyer, R. J., "Modifying structure-sensitive reactions by addition of Zn to Pd", *J. Catal.*, 2014, **318**, 75-84.

[35] Regalbuto, J. R.; Schreier, M.; Hao, X. Spieker, W.A.; Kim, J.G.; Miller, J. T.; Kropf, J. A., "Toward a Molecular Understanding of Noble Metal Catalyst Impregnation," in *Studies in Surface Science and Catalysis, Preparation of Catalysts VIII*, 2002, **143**, 45-53.

[36] Spieker, W. A.; Miller, J. T.; Kropf, A. J., Regalbuto, J.R., "An EXAFS study of the coordination chemistry of hydrogen hexachloroplatinate (IV) 2. Speciation of complexes adsorbed onto alumina", *Appl. Catal. A: Gen.*, 2003, **243**, 53-66.

[37] Yang, C.; Wu, Z.; Zhang, G.; Sheng, H.; Tian, J.; Duan, Z.; Hyuntae, S.; Kropf, A. J.; Wu, T.; Krause, T; Miller, J. T., "Promotion of Pd nanoparticles by Fe and formation of a Pd_3Fe intermetallic alloy for propane dehydrogenation", *Catal. Today*, 2018, **323**, 123-128.

[38] Sheu, L. L.; Karpinski, Z.; Sachtler, W. M. H., "Effects of Palladium Size and Palladium Silicide Formation on Fourier Transform Infrared Spectra of CO Adsorbed on Pd/SiO_2 Catalysts", *J. Phys. Chem.*, 1989, **93**, 4890-4894.

[39] Tereshchenko, A.; Guda, A.; Polyakov, V.; Rusalev, Y.; Butova, V.; Soldatov, A., "Pd nanoparticle growth monitored by DRIFT spectroscopy of adsorbed CO", *Analyst*, 2020, **145**, 7534-7540.

[40] Miller, J. T.; Kropf, A.J.; Zha, Y.; Rebalbuto, J. R.; Delannoy, L.; Louis, C.; Bus, E.; van Bokhoen, J. A., "The effects of gold particle size on Au-Au bond length and reactivity toward oxygen in supported catalysts", *J. Catal.*, 2006, **240**, 222-234.

[41] Srabionyan, V. V.; Bugaev, A. L.; Pryadchenko, V. V.; Avakyan, L. A.; van Bokhoven, J. A.; Bugaev, L. A., "EXAFS study of size dependence of atomic structure in palladium nanoparticles", *J. Phys. Chem. Solids*, 2014, **75**, 470-476.

[42] Purdy, S. C.; Seemakurthi, R. R.; Mitchell, G. M.; Davidson, M.; Lauderback, B. A.; Deshpande, S.; Wu, Z.; Wegener, E. C.; Greeley, J.; Miller, J. T., "Structural trends in the dehydrogenation selectivity of palladium alloys", *Chem. Sci.*, 2020, **11**, 5066-5081.

[43] Szczerba, W.; Riesmeier, H.; Thünemann, A., "Bond length contraction in gold nanoparticles", *Anal. Bioanal.*, 2010, **398**, 1967-1972.

[44] Somorjai, G. A.; Carrazza, J., "Structure sensitivity of catalytic reactions", *Ind. Eng. Chem. Fundamen.*, 1986, **25**, 63-69.

[45] Lear, T.; Marshall, R.; Lopez-Sanchez, J. A.; Jackson, S. D.; Klaptöke, T. M.; Bäumer, M.; Rupprechter, G.; Freund, H.J.; Lennon, D., "The application of infrared spectroscopy to probe the surface morphology of alumina-supported palladium catalysts", *J. Chem. Phys.*, 2005, **123**, 174706.

[46] Yang, F.; LiBretto, N. J.; Komarneni, M. R.; Zhou, W.; Miller, J. T.; Zhu, X.; Resaco, D. E., "Enhancement of *m*-Cresol Hydrodeoxygenation Selectivity on Ni Catalysts by Surface Decoration of MoO_x Species", *ACS Catal.*, 2019, **9**, 7791-7800.

3. THE ROLE OF LEWIS ACID SITES IN Γ-AL_2O_3 OLIGOMERIZATION

3.1 Introduction

Since the original report of olefin oligomerization by Day et al. in 1886 where ethylene was thermally converted to liquid range products at 400 °C,[1] there has been a continued interest in developing oligomerization technology for converting light olefins into value-added products. Early studies focused on understanding thermal reactions at high temperatures. These reactions underwent radical chemistry[2-8] and produced a wide range of products due to oligomerization and thermal cracking[9-21]. Studies transitioned to heterogeneous catalysts such as metallic Pt,[1] metal oxides,[10] and metal chlorides; however,[22] the first commercial breakthrough used solid phosphoric acid (SPA), a Brønsted acid, for the production of gasoline range hydrocarbons. SPA produced primarily C6, C_9, and C_{12} species from propylene through oligomerization and small amounts of other oligomer products through olefin cracking.[23-25] In the 1980's, Mobil developed a process using ZSM-5[26] and Shell developed a process using nickel(II) complexes which were both more active and stable catalysts than SPA.[27] ZSM-5 is a Brønsted acid catalyst that, at low to moderate conversion, produces a mixture of heavy olefin species at 250-400 °C and near-atmospheric pressure due to oligomerization, isomerization, and cracking.[28] High conversion and high pressure Brønsted acids also form aromatic products.[29] Homogenous nickel(II) metal alkyl complexes form primarily linear alpha olefins (LAOs) by the Cosse-Arlman mechanism at 100 °C and >20 bar. This is a highly effective catalyst; however, rapid deactivation occurs above 250 °C due to metallic nickel nanoparticle formation.[30] These catalysts are also readily poisoned by traces of water and oxygen in the feeds.

Recent work by Conrad et al. reported that γ-Al_2O_3 catalyzes olefin oligomerization at 250-450 °C and 1-40 bar with rates that are significantly higher than the thermal reactions.[31] In addition to olefin oligomerization, γ-Al_2O_3 catalyzed additional reactions of double bond isomerization and H-transfer, the latter resulting in a small amount of alkane products. While olefin oligomerization dominates at 20-40 bar resulting in oligomer products (C_{6+}), at near atmospheric pressure, olefin disproportionation results in non-oligomer products such as odd carbon number products from ethylene.[32] Thus, γ-Al_2O_3 is catalytic for oligomerization but gives products that differ

significantly from those typical for Brønsted acid and metal alkyl catalysts. γ-Al_2O_3 is well known to only have Lewis acid sites which were proposed to be the active site for olefin oligomerization.[33-36]

In the present work, the goal is to identify the active sites on γ-Al_2O_3 and to estimate the active site density. The propylene oligomerization conversion was poisoned by addition of Sr^{2+} base. In addition, the catalysts were characterized by X-ray absorption spectroscopy (XAS) at the Sr K edge, STEM, and pyridine infrared (IR) spectroscopy to show that Sr^{2+} single ions are present as isolated ions and lead to a corresponding loss of Lewis acid sites suggesting that these are the catalytic site. The number of Sr^{2+} ions necessary to poison the catalytic activity allows for the determination of the number of active sites.

3.2 Materials and Methods

3.2.1 Materials

CATALOX SBa-200 γ-Al_2O_3 (98%) was purchased from Sasol, strontium nitrate (99%) and strontium oxide (97%) were purchased from Thermo Fisher Scientific, and citric acid (99%) was purchased from Sigma-Aldrich. All gases used for catalytic testing were purchased from Indiana Oxygen Company. The ultra-high purity He (>99.999%) for XAS experiments was purchased from AirGas, Illinois.

3.2.2 Catalyst Preparation

The γ-Al_2O_3 support used was CATALOX SBa-200 (pore size = 4-10 nm, surface area = 200 m^2 g^{-1}, pore volume ~ 0.7 mL/g). XSr/Al_2O_3 catalysts (X wt% Sr) were synthesized using incipient wetness impregnation (IWI). Sr was chosen since this ion has a high enough molecular weight to be imaged by STEM and has a high enough K-edge absorption energy to be characterized by XAS. Varied amounts of strontium nitrate (99%, Thermo Fischer Scientific) corresponding to 0.05-10 wt% Sr were dissolved in ultrapure deionized water (18.2 MΩ-cm). Citric acid (99%, Sigma-Aldrich) was added in a 1:1 molar ratio with strontium nitrate. Ultrapure deionized water was added until fully dissolved. All catalysts were added dropwise to 5g CATALOX SBa-200 γ-

Al_2O_3. The XSr/Al_2O_3 precursors were dried overnight at 125 °C and calcined at a ramp rate of 10 °C/min and held at 550 °C for 3 hours in a convection oven using desiccant dried air.

3.2.3 Low Pressure Propylene Oligomerization

The propylene oligomerization conversion, selectivity, and C_4 product distribution were used to compare the poisoning effect of the Sr base. All catalytic tests were performed in a 12.7 mm ID quartz tube fixed bed reactor with a K-type thermocouple placed in the center of the bed to monitor the reaction temperature. An electrically heated furnace connected to a temperature controller was used to manually adjust the bed temperature. Approximately 2 g of catalyst were loaded into the reactor (supported by quartz wool packed at a constriction in the middle of the tube). The reactions were performed in high purity C_3H_6 (>99.8%) at 425 °C, 1.5 bar, and 10 ccm flowrate. The pressure was maintained using a back pressure regulator in addition to a pressure gauge at the reactor inlet. The products were analyzed after 15 minutes using a Hewlett Packard 6890 GC with a flame ionization detector (FID). There was little deactivation for the duration of the test up to about 1 hour. Peaks were integrated and compared to a bypass run of pure propylene to determine the conversion. Product selectivity and C_4 distributions were determined by subtracting out the impurities present in the high purity C_3H_6 tank (~0.2% C_3H_8). The background thermal conversion was <0.3% for all flow rates.

3.2.4 X-ray Absorption Spectroscopy (XAS)

XAS measurements were conducted at the 10-BM-B beamline at the Advanced Photon Source (APS) of Argonne National Lab (ANL) and at the 8-ID beamline at the National Synchrotron Light Source II (NSLS-II) of Brookhaven National Lab (BNL)[37] at the Sr K edge (16.105 keV) to determine the Sr coordination environment for the 0.05-10 wt% Sr catalysts. At ANL all samples were ground into a fine powder (~20 mg), pressed into a stainless-steel sample holder, sealed in a sample cell (1" OD quartz tube) with Kapton end caps, and scanned as received in 50 ccm flowing ultra-high purity He (>99.999%). At BNL all samples were ground into a fine powder, pressed into wafers, and sealed between Kapton tape. Measurements had a Pb foil (LI edge = 15.861 keV) and a third ion chamber that were used for energy calibrations. XAS data were fit using WinXAS 3.1 software. Least-squares regression fits of the k^2-weighted Fourier transform

data from 2.5 to 10.5 $Å^{-1}$ in k-space were used to obtain the extended x-ray absorption fine structure (EXAFS) coordination parameters. The first shell was used to fit all spectra. All samples were fit using theoretical scattering paths using FEFF software. An S_o^2 value of 0.80 was used for all samples. All samples were analyzed using the same value of σ^2 for direct comparison.

3.2.5 Scanning Transmission Electron Microscopy (STEM)

Samples were dispersed in ethanol (>99.9%, VWR) by grinding with a mortar and pestle. The samples were collected by dipping the TEM grid (part# 3620C-MB, SPI Supplies) under the ethanol mixture and letting the grid dry in air. The samples were analyzed using a JEOL NEOARM 200CF transmission electron microscope equipped with spherical aberration correction to allow atomic resolution imaging, and an Oxford Aztec Energy Dispersive System (EDS) for elemental analysis. The microscope was equipped with two large area JEOL EDS detectors for higher throughput in acquisition of X-ray fluorescence signals. Images were recorded in annular dark field (ADF) mode.

3.2.6 Pyridine infrared (IR) Transmission Spectroscopy

The acid sites of alumina were investigated using transmission IR spectroscopy of adsorbed pyridine. The spectra were collected using a Thermo Fisher Nicolet 4700 spectrometer equipped with a mercury cadmium telluride detector (MCT-A). Each spectra was recorded by collecting 32 scans from 4000 to 650 cm^{-1} at a resolution of 4 cm^{-1}. The samples were pressed into wafers (~0.1 g) and added to the cell (1" OD quartz tube) with Kapton end caps. The samples were dehydrated at 350 °C (10 °C/min) in 50 mL/min pure He for 30 minutes then cooled to 150 °C and the unabsorbed spectra were collected. The samples were then introduced to vacuum (<0.1 torr) prior to dosing pyridine at ~2 torr intervals until surface equilibrium was achieved. The samples were introduced to vacuum to remove physically adsorbed pyridine for 30 minutes then were exposed to 50 mL/min pure He at 150 °C prior to data collection. The unabsorbed spectrum was subtracted from the saturated spectrum for each sample. The spectra were normalized by mass of catalyst.

3.3 Results

3.3.1 Catalyst Synthesis

The γ-Al_2O_3 reference catalyst, CATALOX SBa-200 (pore size = 4-10 nm, surface area = 200 m^2 g^{-1}), was used as received. The XSr/Al_2O_3 catalysts (X wt% Sr) were prepared using incipient wetness impregnation (IWI). Equimolar amounts of strontium nitrate and citric acid were added to deionized water. Citric acid acts as a chelating agent which helps prevent agglomeration of metal ions.[38] The resulting solutions were added dropwise to γ-Al_2O_3. The Sr poison (base) precursors were dried and calcined at 550 °C to remove the organic ligands. The catalysts contained ~0.05-10 wt% Sr.

3.3.2 Low Pressure γ-Al_2O_3 Oligomerization

The conversion of γ-Al_2O_3 and Sr poisoned catalysts for propylene oligomerization was determined at near atmospheric pressure (Figure 1). Reaction products were collected after 15 minutes at 425 °C and 1.5 bar with 2g Al_2O_3 at flow rates of 10-100 ccm C_3H_6. In the absence of a catalyst, the thermal conversion was < 0.3% at all flowrates. The space velocity was varied to give conversions from 6-31% to determine the product selectivity (Figure 2) and C_4 distribution (Figure 3).

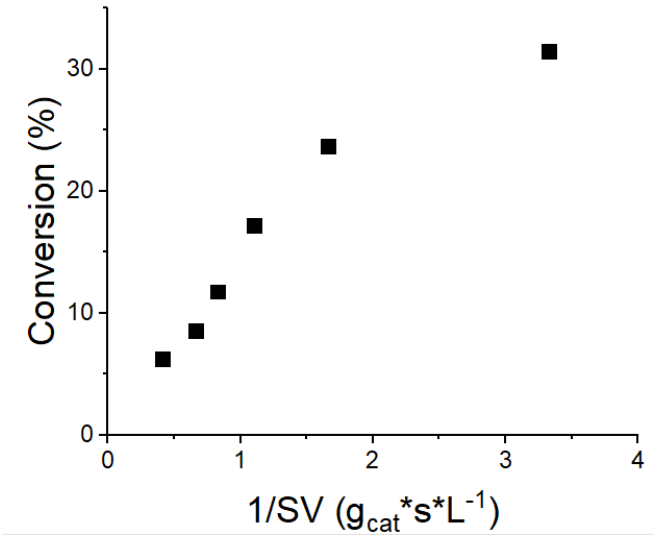

Figure 12. Propylene oligomerization conversion of γ-Al_2O_3 at 425 °C, 1.5 bar, and propylene

The product selectivity was analyzed at each conversion (Figure 2). Similar to the previous study of ethylene oligomerization, non-oligomer C_4 and C_5 products were formed.[31] At all flow rates, there was ~80% selectivity to C_{4-6} species, ~10-20% selectivity to ethylene, and ~5% selectivity to propane. There was < 2% selectivity to methane and only trace amounts of ethane and C_{7+} hydrocarbons. Propane selectivity decreased with increasing conversion. C_4 selectivity was higher and the C_6 selectivity was significantly lower at 31% conversion. All conversions had similar C_5 selectivity.

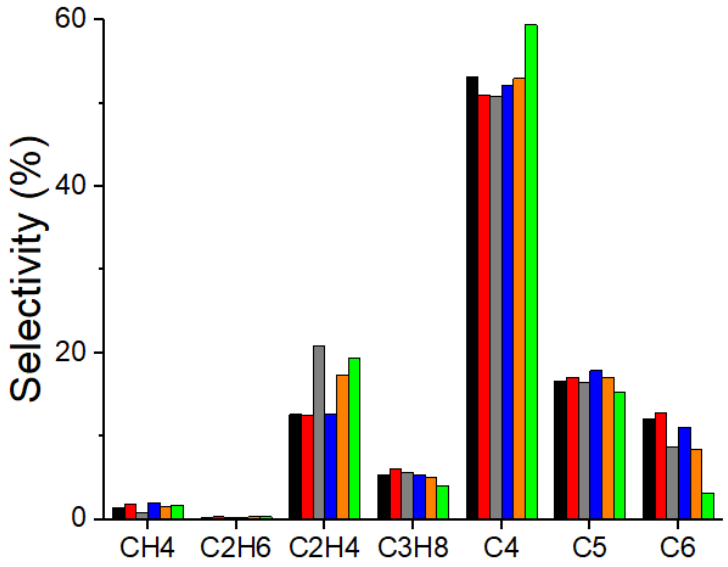

Figure 13. Product selectivity at 6.2% (black), 8.5% (red), 11% (grey), 17% (blue), 24% (orange), and 31% (green) conversion using γ-Al_2O_3 at 425 °C, 1.5 bar, and propylene

The effect of increasing conversion on the C_4 product distribution was determined (Figure 3). Isobutene was the predominant C_4 product at all conversions. As conversion increased, the fraction of isobutene decreased. Generally, all other species correspondingly increased slightly. There were additionally small amounts of other hydrocarbons, e.g., n-butane, isobutane, and butadiene. The reaction products from Figures 1-3 indicate that γ-Al_2O_3 converts propylene with a significant selectivity to non-oligomer C_4 and C_5 products consistent with the previous study.[31]

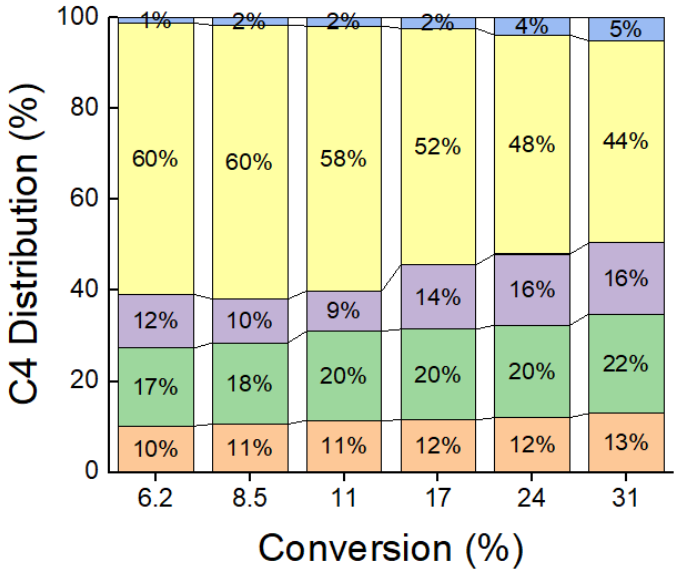

Figure 14. C4 product distribution of 1-butene (red), trans-2-butene (green), cis-2-butene (purple), isobutene (yellow), and other C4 species (blue) at different conversion levels using γ-Al_2O_3 at 425 °C, 1.5 bar, and propylene

3.3.3 Poisoning of γ-Al_2O_3 Using Sr

10 wt% Sr base was added to γ-Al_2O_3 using incipient wetness impregnation (IWI) to poison the catalytic sites. The propylene oligomerization conversion was measured using the same conditions as for γ-Al_2O_3 (2g, 425 °C, 1.5 bar, 10 ccm flowrate) and the product selectivity and C_4 distribution were analyzed. With 10% Sr, the conversion was 0.5% which corresponds to 99% loss of γ-Al_2O_3 catalytic activity (Equation 1). (The thermal background conversion was 0.3%)

Equation 1.

$$\%\ Poison = \left(1 - \frac{X_{Sr/Al_2O_3} - X_{Thermal}}{X_{Al_2O_3} - X_{Thermal}}\right) * 100\%$$

Loadings of 0.05-5 wt% Sr were used to partially poison the γ-Al_2O_3 catalytic activity (Table 1, Figure 4). While γ-Al_2O_3 had 31% conversion, addition of Sr leads to a decrease in conversion. The conversion decreased linearly up to 0.3 wt% Sr. At higher Sr loadings, there was a non-linear loss in conversion (Figure 4a). Equation 1 was used to determine the fractional loss in conversion. >95% of conversion was poisoned above 2 wt% Sr. Below 0.3 wt% Sr, there was a

linear loss in conversion with increasing Sr loading; while higher loadings resulted in non-linear poisoning.

Table 9. Propylene conversion and percent poisoning of XSr/Al_2O_3 catalysts with increasing Sr loading at 425 °C, 1.5 bar and 10 ccm

Sr Loading (wt%)	Conversion (%)	Poison (%)
Thermal	0.3	-
0	31	0
0.05	28	13
0.1	22	30
0.2	16	49
0.3	11	66
0.4	8.5	74
0.5	5.1	85
1	5.0	85
2	1.2	97
5	1.6	96
10	0.5	99

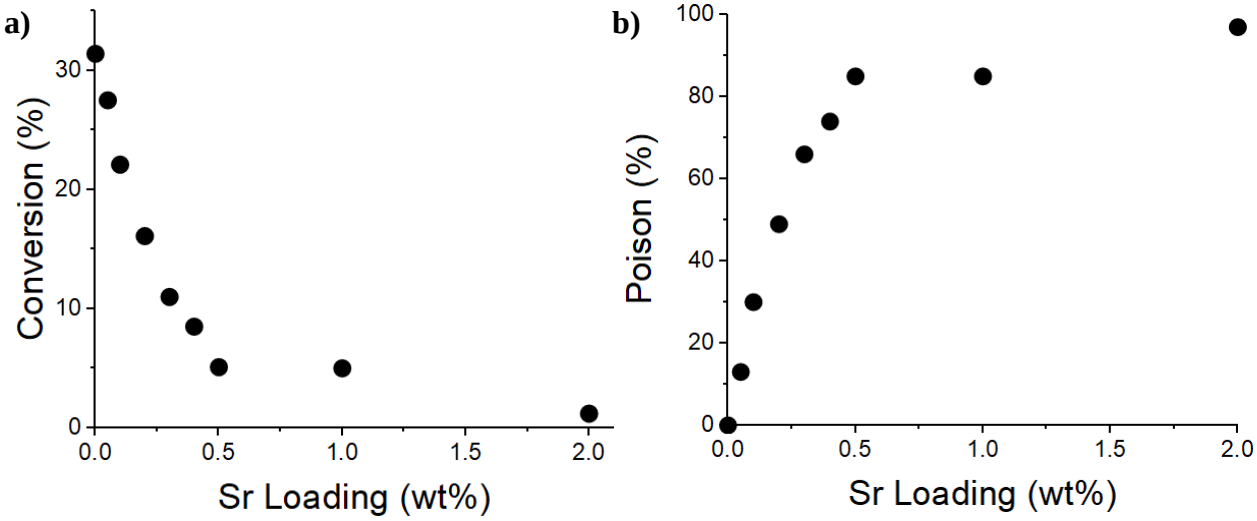

Figure 15. (a) Propylene conversion and (b) percent poisoning of the catalytic activity of XSr/Al_2O_3 catalysts at 425 °C, 1.5 bar, and 10 ccm propylene

The product selectivity and C_4 distribution of $0.4Sr/Al_2O_3$ (26% of active sites remaining) were compared to γ-Al_2O_3 at the same conversion (Figure 5-6). The overall product selectivities were similar. There were minor differences, most notably the C_4 selectivity of $0.4Sr/Al_2O_3$ being

57% compared to 52% for γ-Al_2O_3. The C_5 and C_6 selectivities were both slightly lower for the 0.4Sr/Al_2O_3 catalyst. The C_4 product distribution of both catalysts were identical. This suggests that all active sites are catalytically identical.

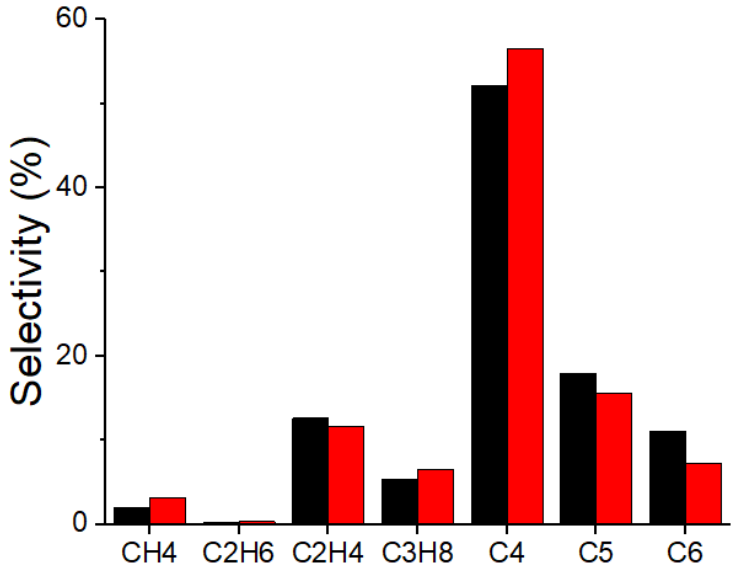

Figure 16. Product selectivity of γ-Al_2O_3 (black) and 0.4Sr/Al_2O_3 (red) at 425 °C, 1.5 bar at ~8.5% conversion

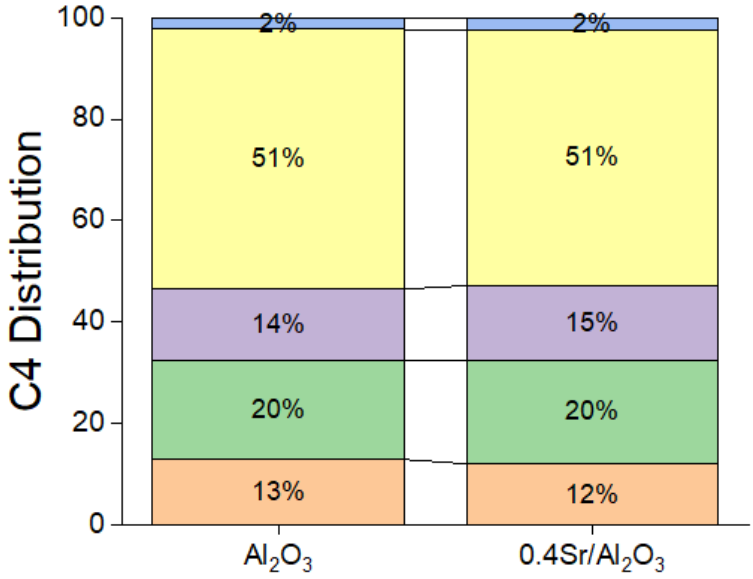

Figure 17. C4 product distribution of 1-butene (red), trans-2-butene (green), cis-2-butene (purple), isobutene (yellow), and other C4 species (blue) of γ-Al_2O_3 and 0.4Sr/Al_2O_3 at 425 °C, 1.5 bar at ~8.5% conversion

3.3.4 Local Structure of the Sr Species

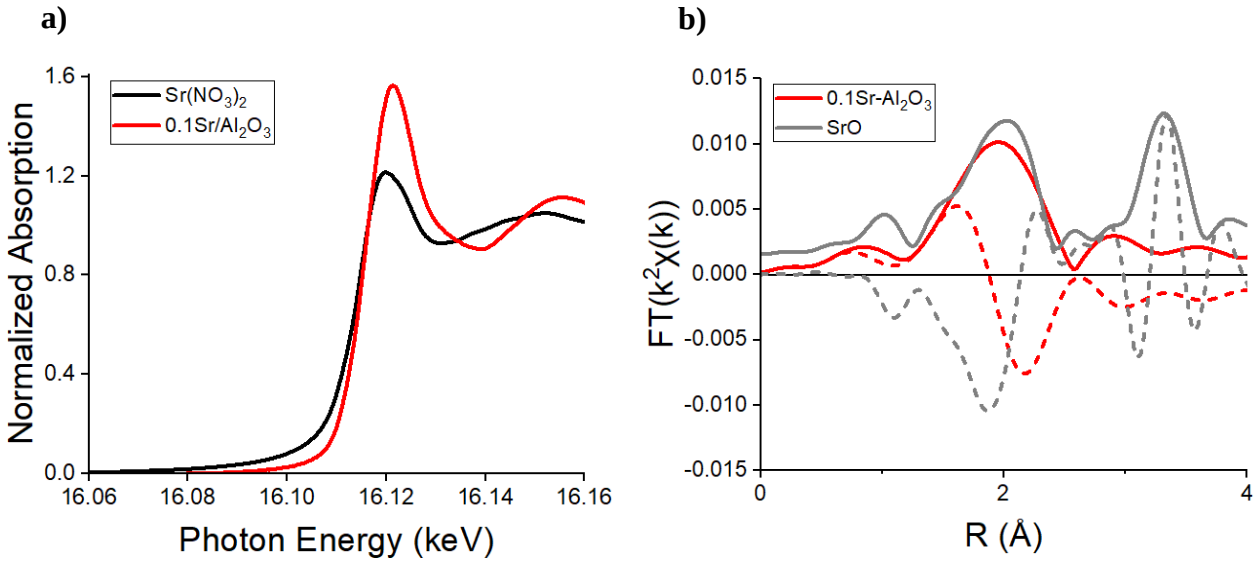

Figure 18. (a) Sr K-edge XANES from 16.06 to 16.16 keV of $Sr(NO_3)_2$ (black) and $0.1Sr/A1_2O_3$ (red) and (b) Fourier transform of the k^2-weighted EXAFS from $\Delta k = 2.5$ to 10.5 $Å^{-1}$ of SrO (grey) and $0.1Sr/Al_2O_3$ (red) scanned in flowing He at 30 °C

The local structure of the Sr species was determined using Sr K-edge XAS and STEM imaging. Sr K edge X-ray absorption spectroscopy was used to determine the Sr oxidation state and coordination environment. Spectra were collected at 30 °C in flowing He. The XANES region was used to determine the edge energy and oxidation state of the Sr samples. Figure 7a shows the XANES of the $Sr(NO_3)_2$ standard and $0.1Sr/Al_2O_3$ from 16.06 to 16.16 keV. The edge energies were 16.1150 and 16.1156 keV, respectively, indicating Sr^{2+} on alumina. The XANES of all Sr/Al_2O_3 catalysts were identical.

The EXAFS was used to determine the coordination environment, for example the number of Sr-O bonds and bond distance, of the Sr atoms. There was one large peak between 1.5-2.4 Å (phase uncorrected distance) for SrO which corresponds to Sr-O first shell scattering. There was a second, larger peak between 2.7-3.7 Å which corresponds to Sr-O-Sr second shell scattering. For $1.0Sr/Al_2O_3$, there was one large peak between 1.2-2.6 Å corresponding to Sr-O first shell scattering. The smaller magnitude of the Fourier transform indicates that there are fewer Sr-O bonds in the Sr/Al_2O_3 catalyst. In the latter, there is also a small peak between 2.6-3.3 Å which has

a different magnitude and imaginary part of the Fourier transform when compared to SrO indicating there are no Sr-O-Sr bonds. The EXAFS of all samples were modeled using FEFF with an S_o^2 of 0.80 and a σ^2 of $4.0*10^{-3}$. All Sr/Al_2O_3 catalysts had ~4 Sr-O bonds at 2.57-2.58 Å (Figure 8, Table 2). This is slightly shorter than the 2.60 Å observed for SrO. This bond contraction is often observed in single ion species bound to the support surface.[39-41] The higher shell peak in the catalysts is likely Sr-O-Al, but was too weak to reliable fit. The XAS data consistent with isolated Sr^{2+} single ions bound to the oxygen atoms of the γ-Al_2O_3 support.

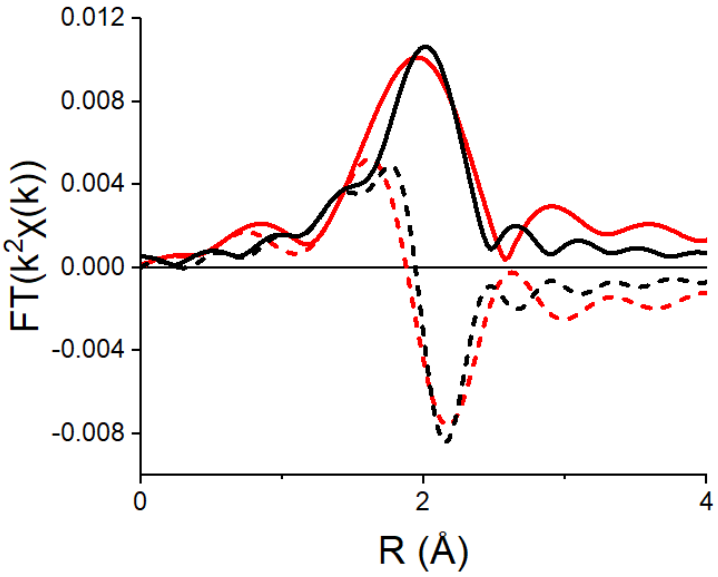

Figure 19. Fourier transform of the k^2-weighted EXAFS from Δk = 2.5 to 10.5 $Å^{-1}$ of $0.1Sr/Al_2O_3$ scanned in flowing He at 30 °C

Table 10. EXAFS fitting parameters for SrO and all XSr/Al_2O_3 catalysts

Sample / Sr Loading (wt%)	**CN_{Sr-O}**	**R (Å)**	**σ^2*10^3 ($Å^2$)**	**E_o Shift (eV)**
SrO	6	2.60	-	-
0.1	4.4	2.58	4.0	-4.5
0.2	4.4	2.57	4.0	-4.7
0.3	4.3	2.57	4.0	-4.4
0.4	4.5	2.58	4.0	-4.5
0.5	4.3	2.58	4.0	-4.7
1	4.2	2.58	4.0	-3.8
2	3.8	2.57	4.0	-3.7
5	3.7	2.57	4.0	-3.3
10	3.9	2.58	4.0	-3.7

EDS and AC-STEM images were collected on the $10Sr/Al_2O_3$ catalyst (Figure 9-10). The EDS elemental compositions (Figure 9) had a range of 6-15 wt% Sr on different γ-Al_2O_3 particles indicating that Sr is not evenly dispersed across the support. High resolution AC-STEM images (Figure 10) indicate that strontium was atomically dispersed on γ-Al_2O_3 and did not form small SrO nanoparticles, which is consistent with the XAS analysis.

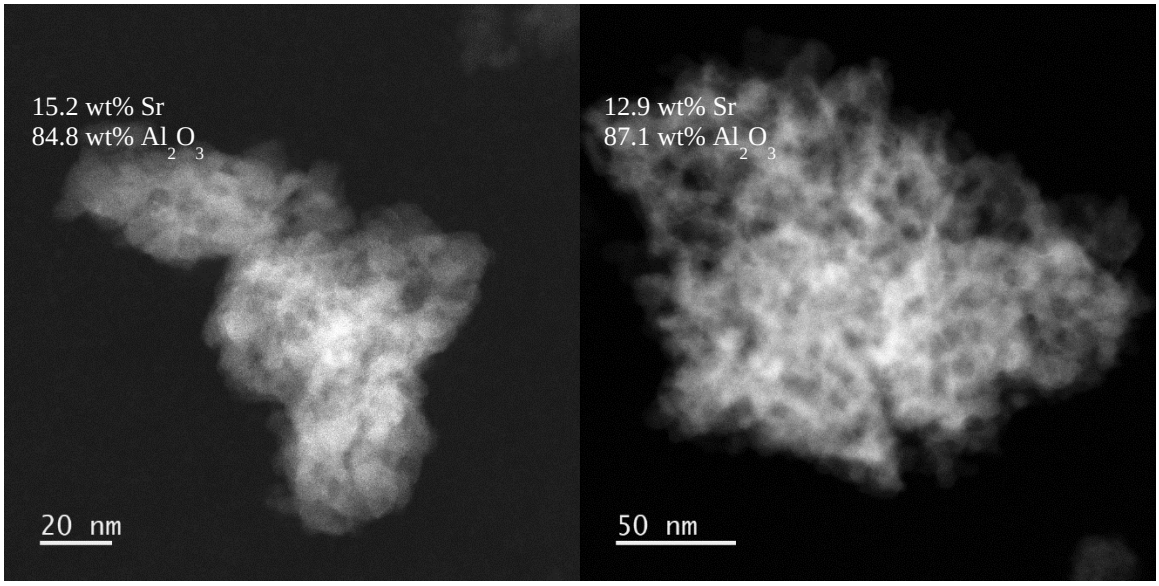

Figure 20. EDS elemental compositions of $10Sr/Al_2O_3$ catalyst particles

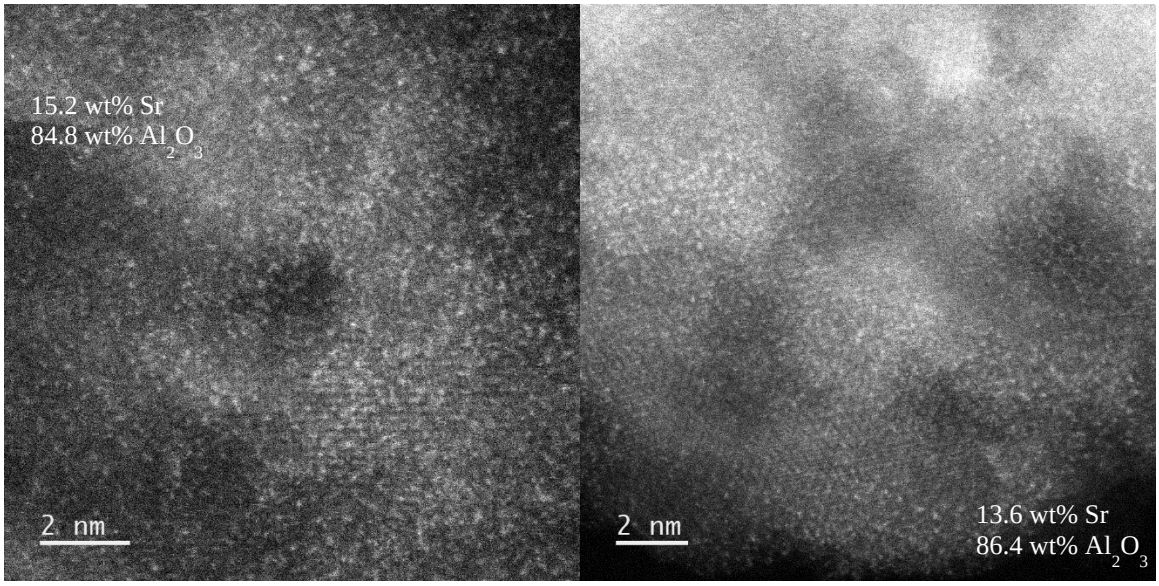

Figure 21. High resolution AC-STEM images of $10Sr/Al_2O_3$ catalyst with EDS compositions

3.3.5 Pyridine infrared spectroscopy

Pyridine infrared spectroscopy (IR) was used to determine the change in the percent of Lewis acid sites present on γ-Al_2O_3 with increasing amounts of added Sr base. The IR spectra of adsorbed pyridine on γ-Al_2O_3 and 10Sr/Al_2O_3 is shown in Figure 11. For γ-Al_2O_3, there were peaks at 1450, 1492, 1575, and 1614 cm^{-1} which have previously been assigned to Lewis acid sites.[33-36] Brønsted acid sites which occur at 1540 cm^{-1} were absent.[33] On the 10Sr/Al_2O_3 catalyst, there were no IR peaks indicating that the Sr addition had poisoned all Lewis acid sites.

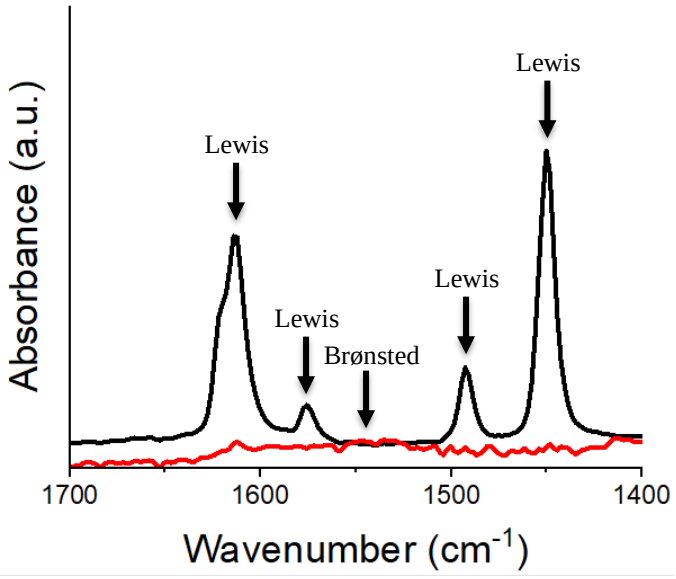

Figure 22. Pyridine IR spectra of γ-Al_2O_3 (black) and 10Sr/Al_2O_3 at 150 °C

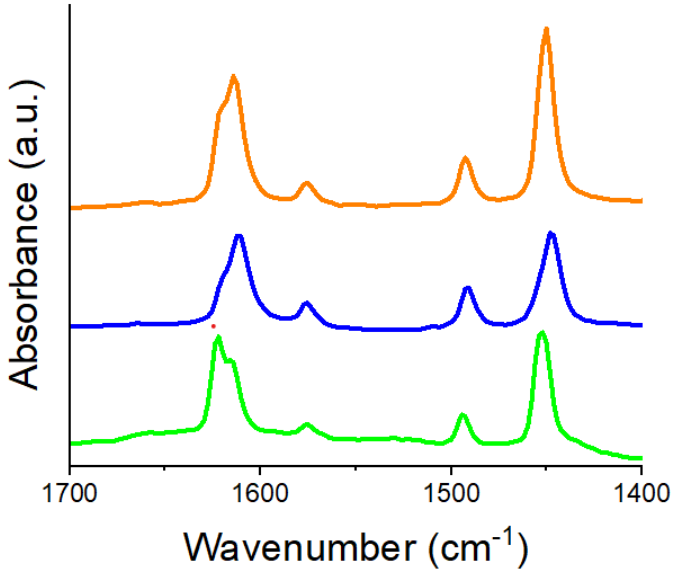

Figure 23. Pyridine IR spectra of 0.05Sr/Al_2O_3 (orange), 0.1Sr/Al_2O_3 (blue), and 0.2Sr/Al_2O_3 (green) at 150 °C

The IR spectra of adsorbed pyridine were obtained for alumina with intermediate loadings (0.05-0.2 wt%) of Sr were obtained to determine if partial Sr coverage leads to partial loss of Lewis acid sites (Figure 12, Table 3). The pyridine IR spectra were similar at all Sr loadings although the peak areas decreased as the Sr loading increased indicating the loss of Lewis acid sites with increasing Sr loading. Equation 2 was used to determine the fractional poisoning of the Lewis acid sites on γ-Al_2O_3. The percent of poisoning for each Sr loading by pyridine IR were also similar to the percent loss in propylene oligomerization conversion indicating that Lewis acid sites are the catalytically active site on γ-Al_2O_3 (Table 3).

Equation 2.

$$\%\ Poison = \left(1 - \frac{Area_{XSr/Al_2O_3}}{Area_{Al_2O_3}}\right) * 100\%$$

Table 11. Poisoning results for select XSr/Al_2O_3 catalysts

Sr Loading (wt%)	Oligo Poison (%)	IR Poison (%)
0	0	0
0.05	13	11
0.1	30	38
0.2	49	56
10	99	100

3.4 Discussion

3.4.1 Identification of the catalytic site on γ-Al_2O_3

Previously, γ-Al_2O_3 was shown to be catalytically active for ethylene oligomerization at high pressure (10-40 atm), and propylene oligomerization is possible at near atmospheric pressure. Since γ-Al_2O_3 is well known to have Lewis acid sites, these were proposed to be the catalytic sites.[31] In this study, the effect of Sr base partial poisoning of γ-Al_2O_3 on the propylene conversion and IR spectra of adsorbed pyridine was determined to confirm that Lewis acid sites are catalytic and to determine the number of active sites. Sr was an effective poison of the catalytic activity (Figure 4) with loadings as low as 2 wt% resulting in near complete loss in conversion. To achieve complete conversion loss, a loading of 10 wt% Sr was required. The poisoning scales linearly up to ~0.3 wt% Sr (66% loss of sites) suggesting that Sr selectively poisons the active sites. At higher loadings, however, Sr was not evenly dispersed across the support as observed by EDS on different γ-Al_2O_3 particles, for example 10 wt% Sr/ Al_2O_3 (Figure 9). As observed in previous study of γ-Al_2O_3, pyridine IR indicates that there are only Lewis acid sites. At 10 wt% Sr there is complete loss of propylene conversion indicating that Lewis acid sites are also the catalytic sites for olefin oligomerization.

3.4.2 The local structure of the Sr^{+2} ions

The local structure of the Sr ions was determined using both XAS and STEM. By XANES, the Sr oxidation state in the XSr/Al_2O_3 catalysts is +2. While the number of Sr-O bonds in SrO is six; the coordination of the Sr ions on γ-Al_2O_3 was four. The absence of Sr-O-Sr scatting from the small higher shell peak in the XSr/Al_2O_3 catalysts indicates that SrO nanoparticles are not formed

and suggests that Sr is present as isolated ions bounded the O ions of the γ-Al_2O_3 surface. This was confirmed by atomic resolution STEM for the 10 wt% Sr/Al_2O_3. Both the XAS and STEM indicate that isolated Sr^{2+} ions can be added to γ-Al_2O_3 up to a loading of 10 wt% Sr.

3.4.3 Determination of the Number of Catalytic Sites on γ-Al_2O_3

The pyridine IR data indicates that there is a decrease in Lewis acid sites with increasing Sr loading. Increasing the Sr loading results in a fractional loss of the number of Lewis acid sites and additionally oligomerization conversion (Table 3) again indicating that Lewis acid sites are the active site on γ-Al_2O_3. The site density can be calculated by extrapolating the linear range of Sr poisoning to a fully covered γ-Al_2O_3 surface. It is estimated that ~0.4 wt% Sr is necessary to poison all catalytic activity. Since XAS and STEM indicate that Sr is present as a single ion, it is likely that one Sr^{2+} ion poisons one catalytic site. Alternatively, one can calculate the loss in the number of active sites in the range where there is a linear loss in conversion with increasing Sr. For example, at 0.3 wt% Sr there is a 66% conversion loss (Table 1). Both methods correspond to ~$4*10^{-5}$ moles Sr per gram of catalyst or ~0.2 Lewis acid sites per nm^2.

3.5 Conclusions

Sr/Al_2O_3 catalysts with 0.05-10 wt% Sr were synthesized using IWI and calcination at 550 °C. These synthesis conditions resulted in single ion Sr^{2+} species bound to the γ-Al_2O_3 support as determined by XAS and STEM. Increasing the Sr loading decreased the propylene oligomerization conversion. Partially poisoned γ-Al_2O_3 had a similar product selectivity and C_4 distribution as γ-Al_2O_3 at the same conversion indicating that all catalytic sites on γ-Al_2O_3 are identical. The Sr poisoned the active sites linearly up to ~0.3 wt%. A loading of >2 wt% Sr was resulted in >95% loss of the olefin conversion. STEM results indicated that the Sr was not evenly dispersed across the γ-Al_2O_3 support. Poisoning of γ-Al_2O_3 by Sr^{2+} ions also lead to a loss in the number of Lewis acid sites by pyridine IR. The loss in oligomerization activity directly correlated with the loss in Lewis acid sites indicating that Lewis acid sites are the active sites on γ-Al_2O_3. Extrapolation of the linear poisoning region suggests that ~0.4 wt% Sr is required to fully poison the Lewis acid sites if Sr was evenly dispersed. This corresponds to ~0.2 Lewis acid sites per nm^2 of γ-Al_2O_3.

3.6 References

[1] Day, D. T., "On the changes effected by heat in the constitution of ethylene", *Am. Chem. J.*, 1886, **8**, 153-167.

[2] Laird, R. K.; Morrell, A. G.; Seed, L., "The velocity of ethylene polymerization at high pressures", *Discuss. Farady Soc.*, 1956, **22**, 126-137.

[3] Dahlgren Jr., G.; Douglas, J. E., "Kinetics of the thermal reactions of ethylene", *J. Am. Chem. Soc.*, 1958, **80**, 5108-5110.

[4] Boyd, M. L.; Wu, T-M.; Back, M. H., "Kinetics of the thermal reactions of ethylene. Part I", *Can. J. Chem.*, 1968, **46**, 2415-2426.

[5] Simon, M.; Back, M. H., "Kinetics of the thermal reactions of ethylene", *Can. J. Chem.*, 1969, **47**, 251-255.

[6] Quick, L. M.; Knecht, D. A.; Back, M. H., "Kinetics of the formation of cyclobutane from ethylene", *Int. J. Chem. Kinet.*, 1972, **4**, 61-68.

[7] Richard, C.; Scacchi, G.; Back, M. H., "Ene reactions of olefins. I. The addition of ethylene to 2-butene and the decomposition of 3-methylpentene-1", *Int. J. Chem. Kinet.*, 1978, **10**, 307-324.

[8] Ayranci, G.; Back M. H., "Kinetics of the bimolecular initiation process in the thermal reactions of ethylene", *Int. J. Chem. Kinet.*, 1981, **13**, 897-911.

[9] Ipatieff, V. N., "Polymerisation der äthylen-kohlenwasserstoffe bei hohen temperaturen und drucken", *Berichte Dtsch. Chem. Ges*, 1911, **44**, 2978–2987.

[10] Walker, H. W., "Catalytic reactions of ethylene", *J. Phys. Chem.*, 1927, **31**, 961–996.

[11] Hurd, C. D., "The pyrolysis of carbon compounds", *J. Soc. Chem. Ind.*, 1929, **48**, 3561-3572.

[12] Pease, R. N., "The non-catalytic polymerization and hydrogenation of ethylene", *J. Am. Chem. Soc.*, 1930, **52**, 1158-1164.

[13] Pease, R. N., "Kinetics of the polymerization of ethylene at pressures above one atmosphere", *J. Am. Chem. Soc.*, 1931, **53**, 613-619.

[14] Dunstan, A. E., "Recent progress in thermal polymerization and condensation of gaseous hydrocarbons", *Trans. Faraday Soc.*, 1936, **32**, 227-234.

[15] Storch, H. H., "Kinetics of ethylene polymerization", *J. Am. Chem. Soc.*, 1935, **57**, 2598-2601.

[16] Frolich, P. K.; Wiezevich, P. J., "Symposium on the chemistry of gaseous hydrocarbons cracking and polymerization of low molecular weight hydrocarbons", *Ind. Eng. Chem.*, 1935, **27**, 1055-1062.

[17] Ingold, K. U.; Stubbs, F. J., "The kinetics of the thermal decomposition of olefins part I. propylene", *J. Chem. Soc.*, 1951, **0**, 1749-1754.

[18] Sullivan Jr., F. W.; Ruthruff, R. F.; Kuentzel, W. E., "Pyrolysis and polymerization of gaseous paraffins and olefins", *Ind. Eng. Chem.*, 1935, **27**, 1072-1077.

[19] Maschwitz, P. A.; Henderson, L. M., "Polymerization of hydrocarbon gases to motor fuels", *Adv. Chem.*, **5**, 83-96.

[20] Molera, M. J.; Stubbs, F. J., "The kinetics of the thermal decomposition of olefins. Part II", *J. Chem. Soc.*, 1952, **0**, 381-391.

[21] Silcocks, C. G., "The kinetics of the thermal decomposition and polymerization of ethane and ethylene", *R. Soc.*, 1956, **223**, 465-479.

[22] Ipatieff, V. N.; Grosse, A. V., "Polymerization of ethylene with aluminum chloride", *J. Am. Chem. Soc.*, 1936, **58**, 915-917.

[23] Egloff, G.; Lowry Jr., C. D.; Schaad, R. E., "Polymerization and decomposition of acetylene hydrocarbons", *J. Phys. Chem.*, 1932, **36**, 1457-1520.

[24] Egloff, G.; Wilson, E., "Thermal reactions of gaseous hydrocarbons", *Ind. Eng. Chem.*, 1935, **27**, 917-933.

[25] Egloff, G., "Gasoline and lubricating oil", *Sci. Mon.*, 1933, **37**, 218-220.

[26] Quann, R. J.; Green, L. A.; Tabak, S. A.; Krambeck, F. J., "Chemistry of olefin oligomerization over SZM-5 catalyst", *Ind. Eng. Chem. Res.*, 1988, **27**, 565-570.

[27] Peuckert, M.; Keim, W., "A new nickel complex for the oligomerization of ethylene", *Organometallics*, 1983, **2**, 594-597.

[28] Garwood, W. E., 1983, "Conversion of C2-C10 to Higher Olefins over Synthetic Zeolite ZSM-5", ACS Symposium Series, Am. Chem. Soc., Washington, DC, United States.

[29] Bhan, A.; Delgass, W. N., "Propane aromatization over HZSM-5 and Ga/HZSM-5 Catalysts", *Catal. Rev.*, 2008, **50**, 19-151.

[30] Finiels, A.; Fajula, F.; Hulea, V., "Nickel-based solid catalysts for ethylene oligomerization – a review", *Cat. Sci. Technol.*, 2014, **8**, 2412-2426.

[31] Conrad, M. A.; Deline, J. E.; Miller, J. T., "High temperature conversion of olefins to liquid hydrocarbons on γ─Al_2O_3", *Ind. Eng. Chem. Res.*, 2023, 10.1021/acs.iecr.2c02759

[32] Banks, R. L.; Bailey, G. C., "Olefin disproportionation", *Ind. Eng. Prod. Res. Dev.*, 1964, **3**, 170-173.

[33] Parry, E. P., "An infrared study of pyridine adsorbed on acidic solids. Characterization of surface acidity", *J. Catal.*, 1963, **2**, 371-379.

[34] Zaki, M. I.; Hasan, M. A.; Al-Sagheer, F. A.; Pasuplety, L., "In situ FTIR spectra of pyridine adsorbed on SiO_2-Al_2O_3, TiO_2, ZrO_2, and CeO_2: general considerations for the identification of acid sites on surfaces of finely divided metal oxides", *Colloids Surf. A Physicochem. Eng. Asp.*, 2001, **190**, 261-274.

[35] Penkova, A.; Bobadilla, L. F.; Sarria-Romero, F.; Centeno, M. A.; Odriozola, J. A., "Pyridine adsorption on NiSn/MgO-Al_2O_3: an FTIR spectroscopic study of surface acidity", *Appl. Surf. Sci.*, 2014, **317**, 241-251.

[36] Zholobenko, V.; Freitas, C.; Jendrlin, M.; Bazin, P.; Travert, A.; Thibault-Starzyk, F., "Probing the acid sites of zeolites with pyridine: quantitative AGIR measurements of the molar absorption coefficients", *J. Catal.*, 2020, **385**, 52-60.

[37] Leshchev, D.; Rakitin, M.; Luvizotto, B.; Kadyrov, R.; Ravel, B.; Attenkofer, K.; Stavitski, E., "The Inner Shell Spectroscopy beamline at NSLS-II: a facility for in situ and operando X-ray absorption spectroscopy for materials research", *J. Synchrotron Rad.*, 2022, **29**, 1095-1106.

[38] Wei, Q.; Zhou, Y.; Xu, C.; Liu, Y., "Effects of citric acid as a chelating agent on the performance of a heavy oil hydrotreatment catalyst", Chapter 1, *Production and Purification of Ultraclean Transportation Fuels*, 3-13, 2011.

[39] LiBretto, N. J.; Xu, Y.; Quigley, A.; Edwards, E.; Nargund, R.; Vega-Vila, J. C.; Caulkins, R.; Saxena, A.; Gounder, R.; Greeley, J.; Zhang, G.; Miller, J. T., "Olefin oligomerization by main group Ga^{3+} and Zn^{2+} single site catalysts on SiO_2", *Nat. Comm.*, 2021, **12**, 2322.

[40] Ma, R.; Gao, J.; Dean, D.; Breckner, C.; Liang, K.; Zhou, B.; Miller, J.; Zou, G.; "Insights into the nature of selective nickel sites on Ni/Al_2O_3 catalysts for propane dehydrogenation", *ACS Catal.*, 2022, **12**, 12607-12616.

[41] Zelinsky, R.; Dean, D. P.; Breckner, C. J.; Miller, J. T.; Epling, W. S., “Pd/BEA hydrocarbon traps: effect of hydrothermal aging on trapping properties and Pd speciation,”*Appl. Catal. B*, 2023, **320**, 121938.

4. FUTURE DIRECTIONS

The work in this thesis helps advance the development of innovative dehydrogenation and oligomerization catalysts. Lewis acid sites were shown to be an effective oligomerization catalyst on γ-Al_2O_3. This provides research opportunity for the development of other Lewis acid catalysts such as single site transition metal ions supported on γ-Al_2O_3.

Various single sites supported on γ-Al_2O_3 (CATALOX SBa-200) were tested for propylene oligomerization conversion and selectivity. 10X/Al_2O_3 catalysts (10 wt% X, X = Ce/Co/Cr/Cu/Fe/In/La/Mg/Mn/Ni/Y/Yb/Zn) were synthesized using incipient wetness impregnation (IWI). Varied amounts of metal nitrate (98-99% purity) corresponding to 10 wt% metal were dissolved in deionized water. Citric acid (99%) was added in a 1:1 molar ratio with Sr. Deionized water was added until fully dissolved. All catalysts were added dropwise to CATALOX SBa-200 γ-Al_2O_3. The 10X/Al_2O_3 precursors were dried overnight at 125 °C and calcined at 550 °C for 3 hours. The propylene oligomerization conversion, selectivity, and C4 product distribution were used to compare the activity of 10X/Al_2O_3 catalysts to γ-Al_2O_3. All catalytic tests were performed in the same setup and manner as in chapter 3. The reactions were performed with 2 g of catalyst in pure C_3H_6 at 425 °C, 1.5 bar, and 10 ccm flowrate.

The conversion and C4 product distribution of 10X/Al_2O_3 catalysts for propylene oligomerization were determined at 425 °C and near atmospheric pressure (Table 12). The group 2 and 3 metals (Mg, Y, La, Yb) have very low conversion and are thus poor catalysts. The exception to this is Ce which has a similar conversion and C4 product distribution as γ-Al_2O_3. The first row transition metals varied in conversion. Fe had the lowest conversion at 4%. Co, Cu, Mn, and Zn all had conversions of 17-36%. There C4 distributions were significantly different. Co and Zn had ~80% isobutene and <10% of all other species. Cu had only 53% isobutene and had 11-18% for all other C4 olefins. Mn had 37% isobutene and 16-27% for all other C4 olefins. Ni and Cr had the highest conversions at 88 and 74%, respectively. The C4 distributions, however, contained far more alkane species than other catalysts indicating a high hydrogenation activity. This is an undesired property for oligomerization catalysts as rapid hydrogenation prevents

conversion to higher molecular weight liquid products. In was the most interesting catalyst as it had the same conversion as γ-Al_2O_3 but the C4 distribution was exclusively isobutene. The overall selectivity of the oligomerization catalysts with >10% conversion and low hydrogenation activity were further analyzed (Ce, Co, Cu, In, Mn, and Zn).

Table 12. Conversion and C4 product distribution of 10M/Al_2O_3 catalysts at 425 °C and 1.5 bar in 10 ccm propylene

Metal	Conversion (%)	1-Butene (% C4)	Trans-2-Butene (% C4)	Cis-2-Butene (% C4)	Isobutene (% C4)	Other C4 (% C4)
Ce	25	15	26	19	39	1
Co	35	4	6	5	80	5
Cr	74	10	17	12	25	36
Cu	17	11	18	13	53	5
Fe	4	7	12	9	70	2
In	34	<1	<1	<1	99	<1
La	2	4	8	5	82	1
Mg	2	2	4	3	90	1
Mn	25	16	27	19	37	1
Ni	88	12	3	<1	4	81
Y	2	5	9	6	79	1
Yb	7	7	14	9	69	1
Zn	36	5	9	6	79	1

The propylene oligomerization product selectivity of the γ-Al_2O_3 and 10M/Al_2O_3 (M = Ce, Co, Cu, In, Mn, and Zn) catalysts were compared at roughly the same conversions (25-36%) except for Cu which was at 17% conversion. The Ce catalyst had significantly less propane and C4 products but had more C5 and twice as much C6 products as γ-Al_2O_3. The Co catalyst had ~20% methane and ~45% propane. The selectivity to oligomerization products (C4+) was <40%. Similarly, the Cu catalyst had high methane and propane selectivity with reduced C4+ selectivity when compared to γ-Al_2O_3. The In catalyst had ~30% methane and ~70% C4 species which were exclusively isobutene. The Mn catalyst had ~10% methane, ~25% C5, and ~20% C6 products which were all significantly higher than γ-Al_2O_3 while there was significantly less ethylene and C4 species. The Zn catalyst had ~70% methane indicating that it was a poor oligomerization catalyst that favors cracking reactions at these temperatures. Thus, the Ce, Cu, and Mn catalyst were the most effective oligomerization catalysts under these conditions. The In catalyst had the most unique distribution which warrants future studies.

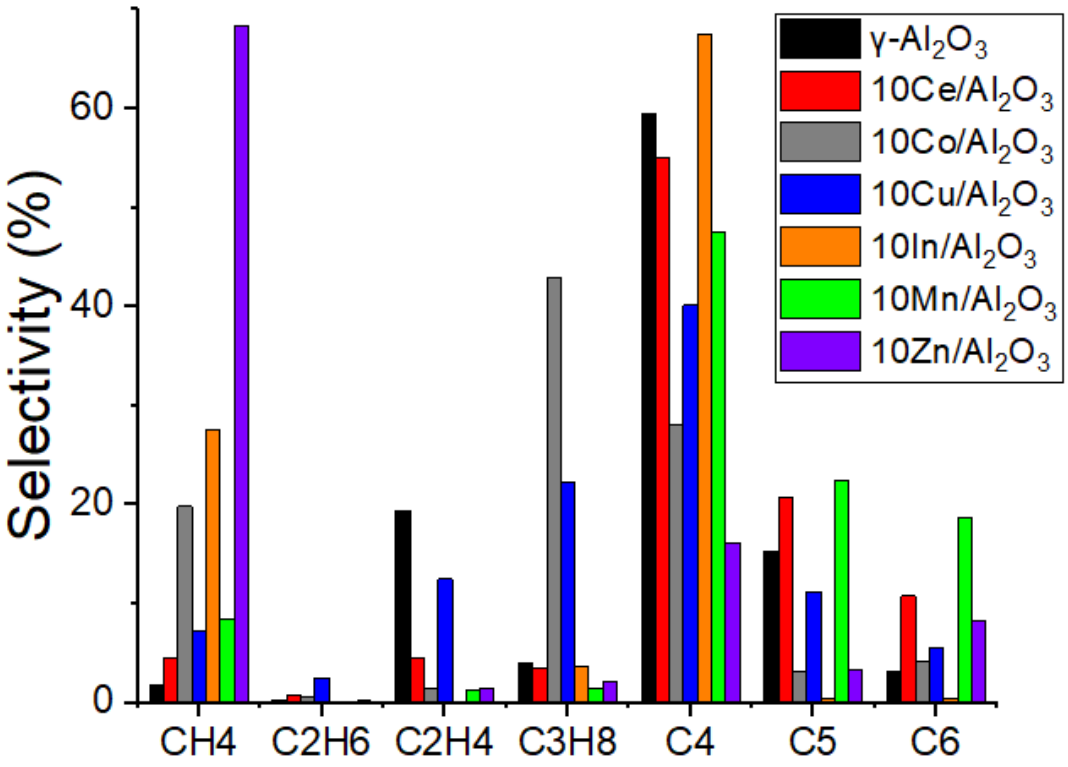

Figure 24. Product selectivity of γ-Al_2O_3 and different 10X/Al_2O_3 catalysts at 425 °C, 1.5 bar, and 10 ccm propylene feed

The Ce, Cu, In, Mn, and Zn containing catalysts should be further tested at high pressure to determine their oligomerization properties under industrially relevant conditions. In addition, characterization using XAS is recommended to determine the oxidation state and coordination environment as these may be single sites, oxide clusters, or metallic nanoparticles. STEM images can be obtained to confirm this. In addition, the pyridine IR spectra of these catalysts should be collected to determine if the single sites are Lewis acid sites. Additional work could look at X-Sr/Al_2O_3 catalysts where the Sr single sites are added first to poison the γ-Al_2O_3 Lewis acid sites. A single site metal could then be added at lower loadings to isolate its catalytic properties.

APPENDIX. SUPPORTING INFORMATION FOR CHAPTER 2

Figures S1-S3 show the Fourier transform of $k^2\chi(k)$ EXAFS scans of the 0.1, 0.5, and 1.0 wt% Ti containing catalysts after 450 °C calcination and 250/400/500/550 °C reduction. All have similar peak shapes characteristic of Pd. They also show similar trends where increasing the reduction temperature increases the height of the peak which corresponds to increasing Pd-Pd coordination and particle size.

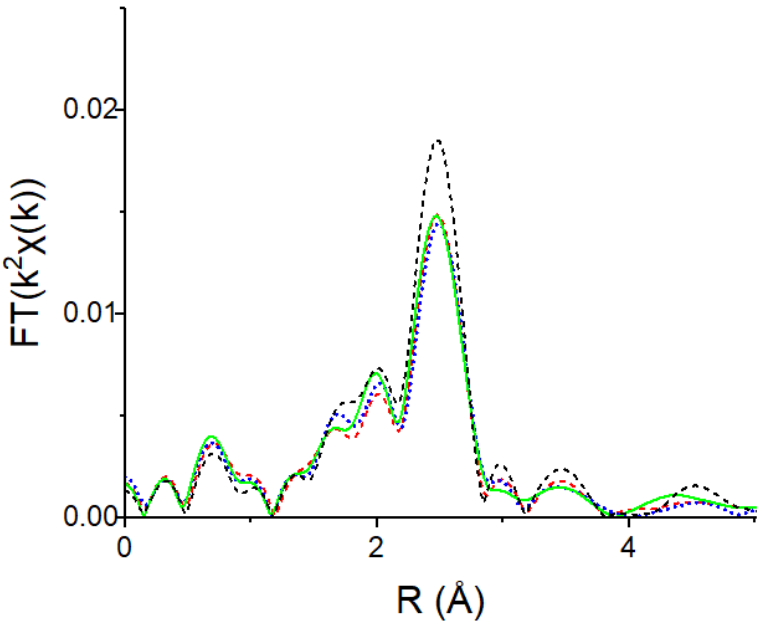

Figure S1. Pd K edge EXAFS spectra for the 0.1 wt% Ti containing catalyst reduced at 250 (red, dash), 400 (blue, dot), 500 (green, solid), 550 (black, dash)

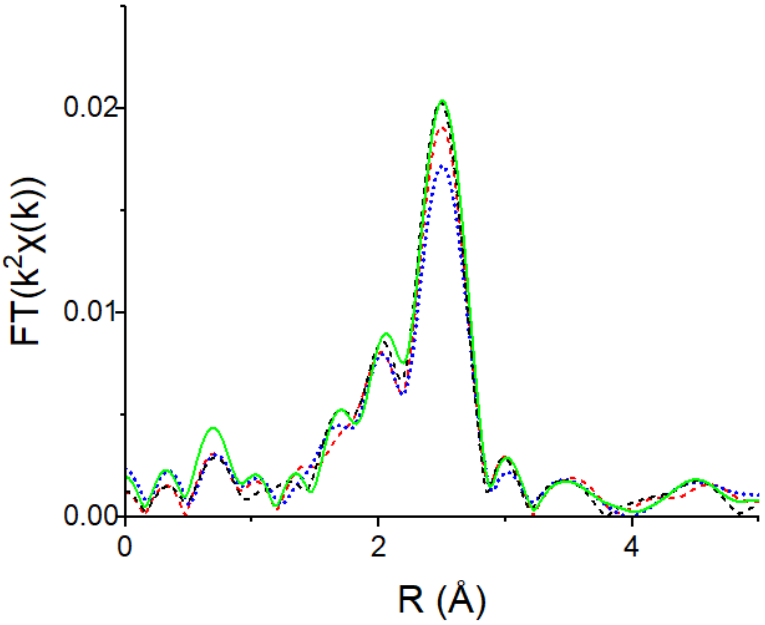

Figure S2. Pd K edge EXAFS spectra for the 0.5 wt% Ti containing catalyst reduced at 250 (red, dash), 400 (blue, dot), 500 (green, solid), 550 (black, dash)

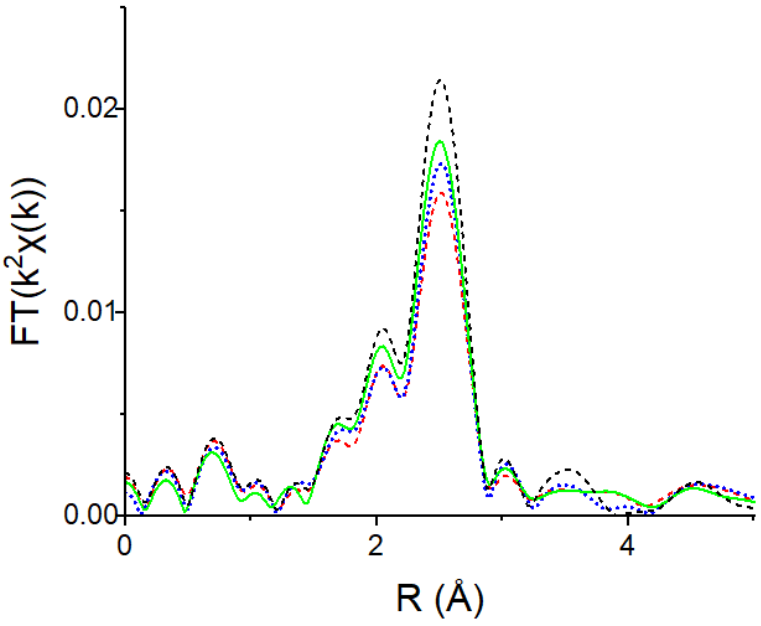

Figure S3. Pd K edge EXAFS spectra for the 1.0 wt% Ti containing catalyst reduced at 250 (red, dash), 400 (blue, dot), 500 (green, solid), 550 (black, dash)

Table S1 includes the fitting parameters of all samples after calcination at 450 °C and reduction at 200/400/500/550 °C. All samples show similar trends where increasing reduction temperature increased the Pd-Pd coordination and particle size most notably after 500 and 550 °C.

Table S1. EXAFS fitting parameters for Pd foil and all catalysts calcined at 450 °C and reduced at different temperatures

Sample / Ti Loading (wt%)	**Reduction Temperature (°C)**	**CN_{Pd-Pd}**	**R (Å)**	**$\Delta\sigma^2$ (Å^2)**	**E_o Shift (eV)**	**Surface Fraction Pd**	**Est. Size (nm)**
Pd Foil	-	12	2.75	0	0	-	-
0	250	5.1	2.74	0.0045	-3.4	0.83	1.2
	400	5.4	2.74	0.0045	-2.8	0.76	1.3
	500	5.9	2.73	0.0040	-2.6	0.65	1.5
	550	6.0	2.73	0.0040	-2.7	0.63	1.6
0.1	250	4.9	2.73	0.0045	-2.7	0.88	1.1
	400	4.8	2.72	0.0045	-3.4	0.90	1.1
	500	5.1	2.73	0.0045	-2.2	0.83	1.2
	550	6.1	2.72	0.0040	-3.6	0.61	1.6
0.5	250	6.1	2.73	0.0040	-3.9	0.61	1.6
	400	5.9	2.73	0.0040	-3.6	0.65	1.5
	500	6.5	2.73	0.0040	-4.1	0.54	1.8
	550	7.1	2.73	0.0040	-3.6	0.45	2.2
1.0	250	5.6	2.74	0.0040	-2.4	0.71	1.4
	400	5.7	2.73	0.0040	-3.4	0.69	1.4
	500	6.6	2.73	0.0040	-3.3	0.53	1.9
	550	7.2	2.74	0.0040	-3.6	0.44	2.3

Figures S4-S9 show the STEM images and the particle size distributions for all catalysts after 450 °C calcination and 550 °C reduction and after subsequent oxidation at 350 °C and re-reduction at 200 C for the 0.1-1.0 wt% Ti containing catalysts. All catalysts had similar average particle sizes with the majority of nanoparticles being 1-3 nm. There were small amounts of larger nanoparticles (4-6.5 nm) present in all catalysts.

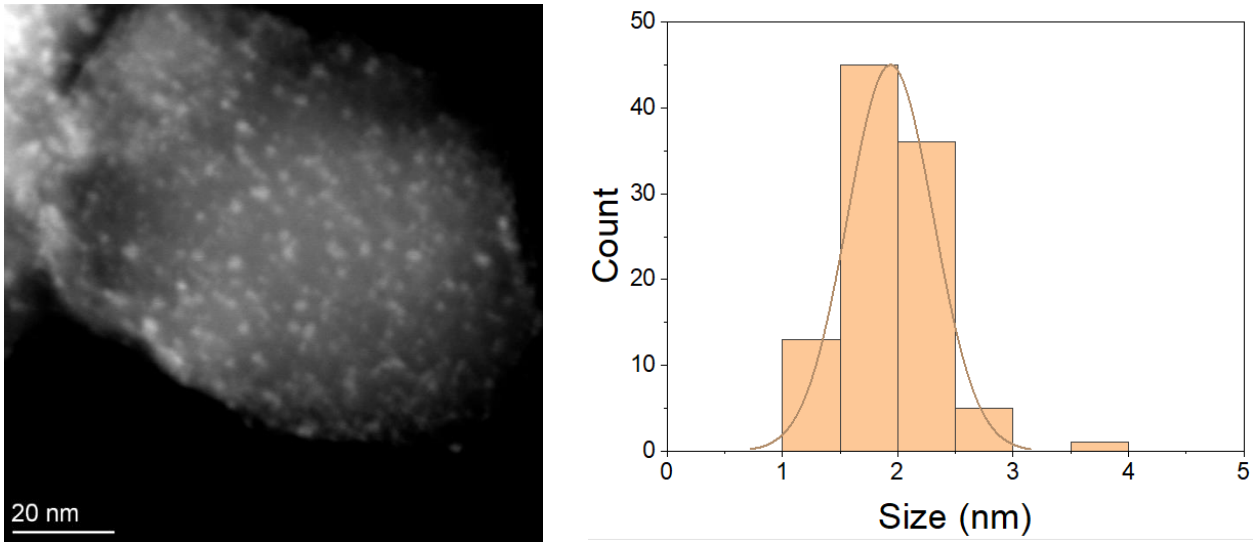

Figures S4. STEM image and particle size distribution of the 0 wt% Ti containing catalyst after 550 °C reduction

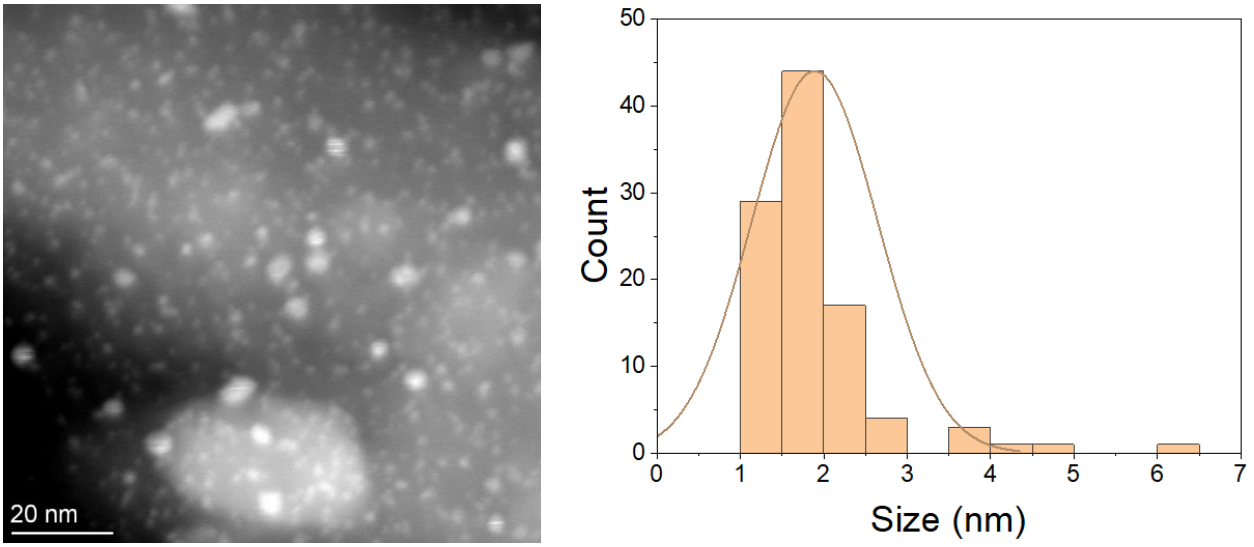

Figures S5. STEM image and particle size distribution of the 0.1 wt% Ti containing catalyst after 550 °C reduction

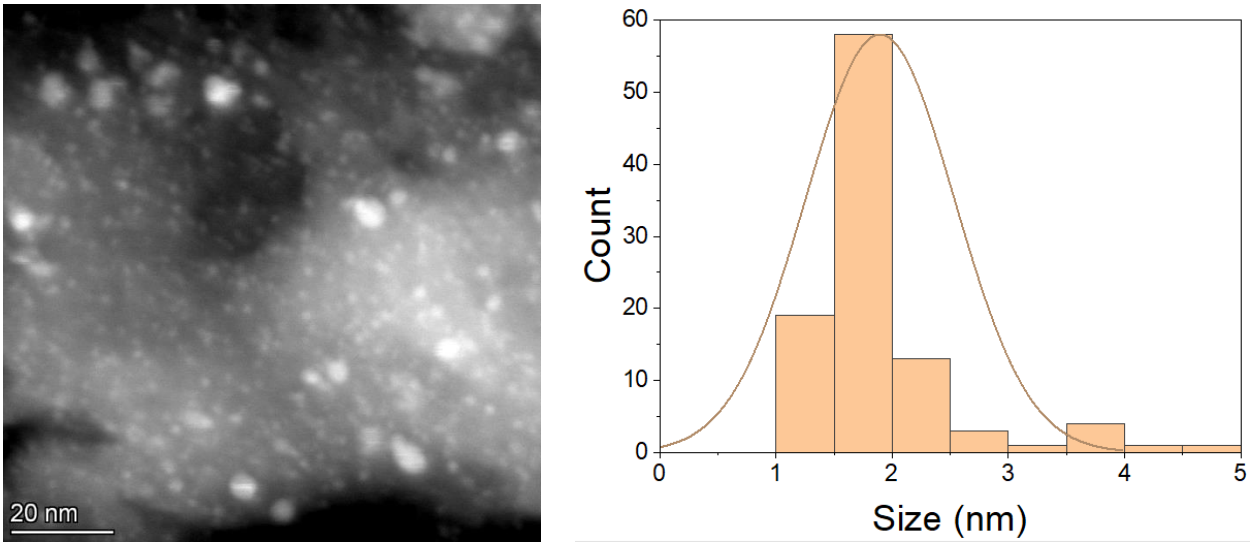

Figures S6. STEM image and particle size distribution of the 1.0 wt% Ti containing catalyst after 550 °C reduction

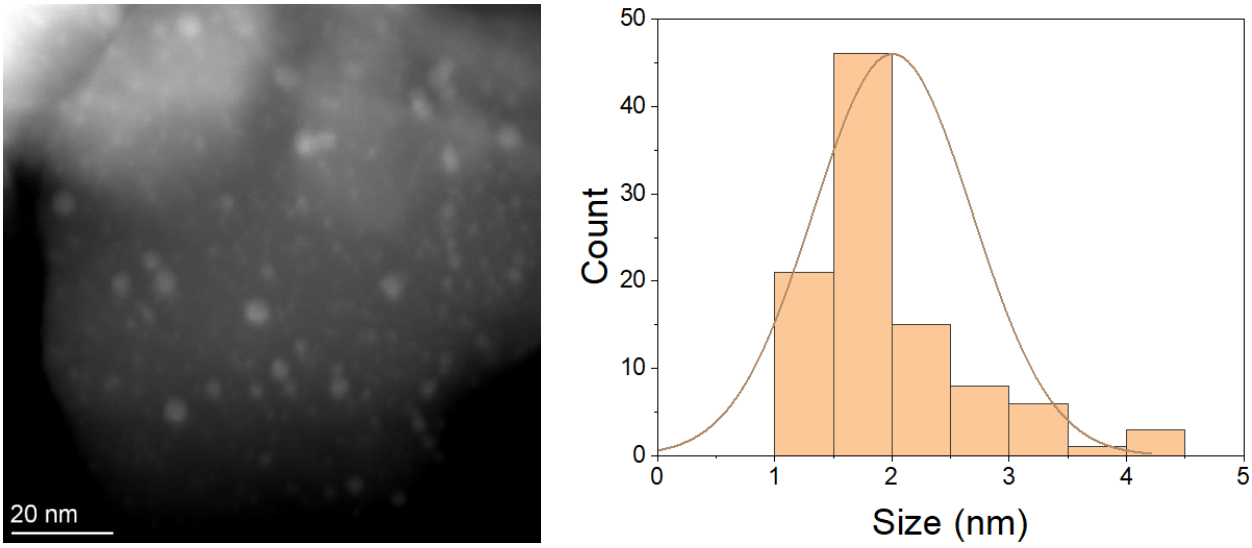

Figures S7. STEM image and particle size distribution of the 0.1 wt% Ti containing catalyst after 550 °C reduction, 350 °C oxidation, and 200 °C re-reduction

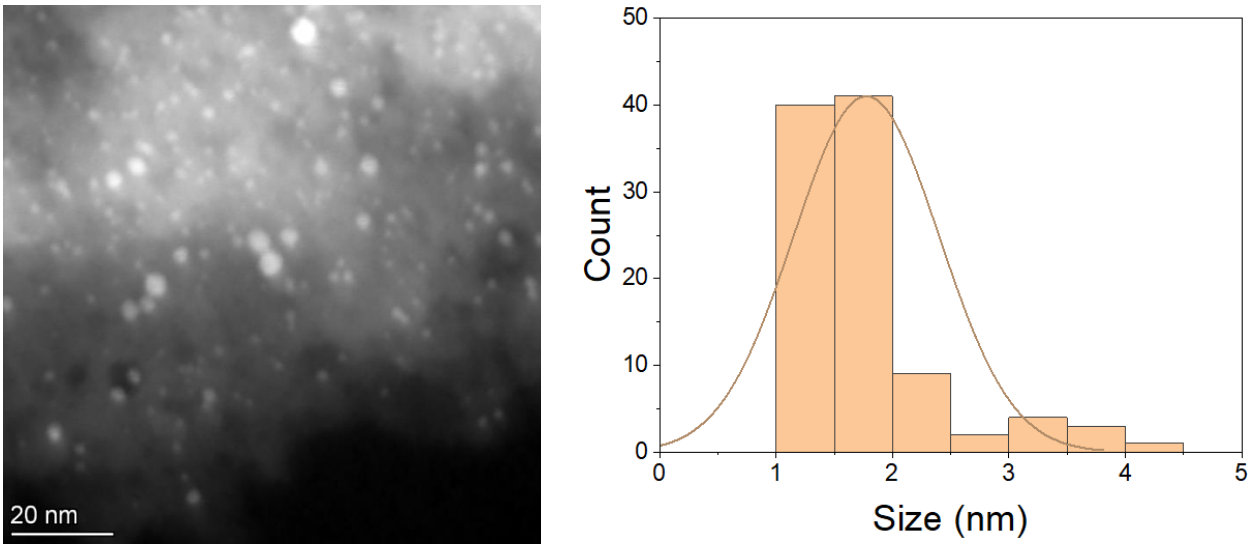

Figures S8. STEM image and particle size distribution of the 0.5 wt% Ti containing catalyst after 550 °C reduction, 350 °C oxidation, and 200 °C re-reduction

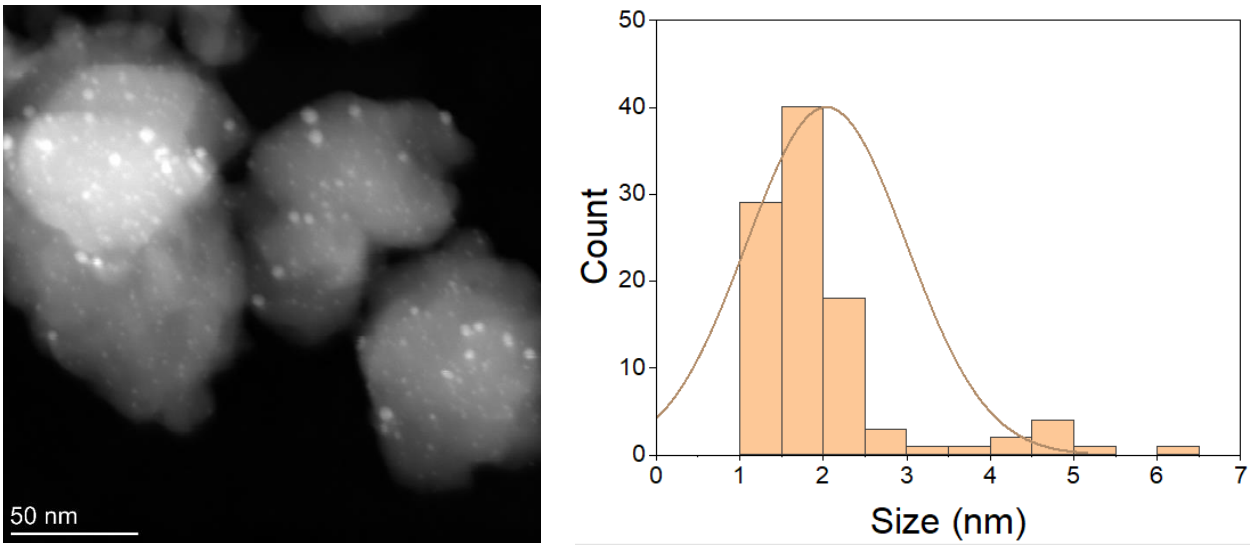

Figures S9. STEM image and particle size distribution of the 1.0 wt% Ti containing catalyst after 550 °C reduction, 350 °C oxidation, and 200 °C re-reduction

Table S2 includes the data used to calculate the estimated TORs in Figure 4.

Table S2. Estimated TOR of catalysts after reduction at 550 °C

Ti Loading (wt%)	**Rate (mol C_3H_8*mol_{metal}^{-1}*s^{-1})**	**Surface Fraction Pd**	**Estimated TOR (s^{-1})**
0	2.6	0.64	4.0
0.1	1.6	0.57	2.5
0.5	0.8	0.44	1.8
1.0	0.4	0.44	0.9

Table S3 includes the catalytic rates that were used to calculate the coverages in Figure 6. All coverages were determined as follows: $Coverage = (1 - \frac{SMSI\ Rate}{Non{-}SMSI\ Rate}) * 100\%$

Table S3. Coverage of SMSI catalysts after reduction at 550 °C

Ti Loading (wt%)	**SMSI Rate (mol C_3H_8*mol_{metal}^{-1}*s^{-1})**	**Non-SMSI Rate (mol C_3H_8*mol_{metal}^{-1}*s^{-1})**	**Coverage (%)**
0.1	1.6	2.7	40
0.5	0.8	3.1	75
1	0.4	2.7	84
6	0.3	2.5	87

Table S4 includes the EXAFS fits of all catalysts after 550 °C reduction (550R), 350° C oxidation, and 200 °C re-reduction (200RR). All had similar peaks characteristic of Pd. All coordination numbers were consistent within ± 0.3 which is within the 10% error commonly used for EXAFS fittings.

Table S4. EXAFS fitting results for catalysts reduced at 550 °C (550R), oxidized at 350 °C, and re-reduced at 200 °C (200RR)

Ti Loading (wt%)	Treatment Step & Scan Conditions	CN_{Pd-Pd}	R (Å)	$\Delta\sigma^2$ (Å^2)	E_o Shift (eV)	Dispersion	Est. Size (nm)
0	550R, He	6.0	2.73	0.0040	-2.8	0.63	1.6
	550R, H_2	6.1	2.75	0.0040	-2.3	0.61	1.6
	200RR, He	5.8	2.72	0.0040	-1.1	0.67	1.5
0.1	550R, He	6.1	2.72	0.0040	-3.6	0.61	1.6
	550R, H_2	6.4	2.75	0.0040	-1.5	0.56	1.8
	200RR, H_2	6.6	2.73	0.0040	-1.9	0.53	1.9
0.5	550R, He	7.1	2.73	0.0040	-1.3	0.45	2.2
	550R, H_2	7.2	2.75	0.0040	-0.7	0.44	2.3
	200RR, H_2	7.3	2.73	0.0040	-1.9	0.43	2.3
1.0	550R, He	7.2	2.74	0.0040	-3.6	0.44	2.3
	550R, H_2	7.1	2.75	0.0040	-2.4	0.45	2.2
	200RR, H_2	7.2	2.73	0.0040	-3.1	0.44	2.3

Figures S10-S12 show the Fourier transform of $k^2\chi(k)$ from EXAFS scans of the 0.1, 0.5, and 1.0 wt% Ti containing catalysts after 550 °C reduction and 30° C oxidation. All have similar peaks characteristic of Pd and PdO. There is increasing peak height and area of the PdO peak as Ti loading is decreased which indicates increasing PdO coordination.

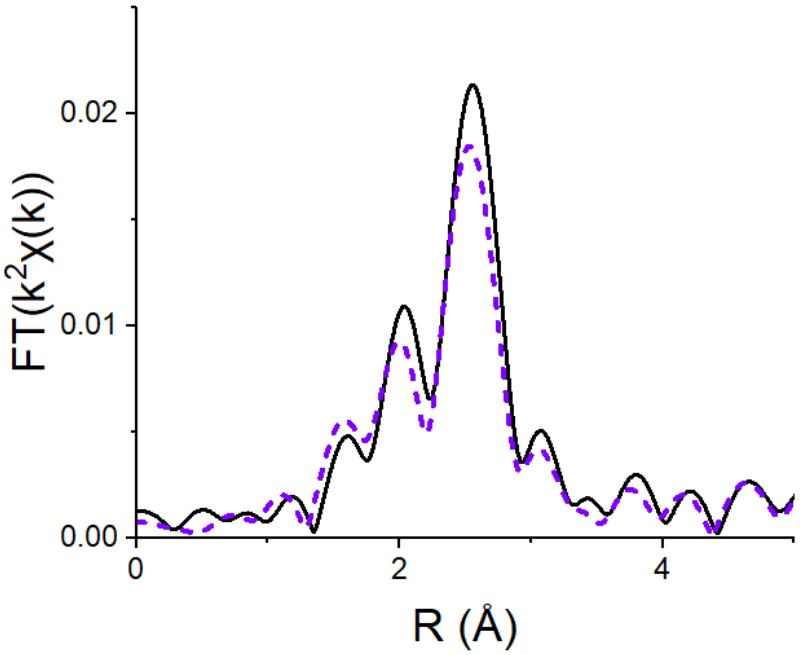

Figure S10. k^2-weighthed Fourier transform of the Pd K edge EXAFS spectra of the 0.1 wt% Ti containing catalyst reduced at 550 °C (black, solid) then oxidized at 30 °C (purple, dash)

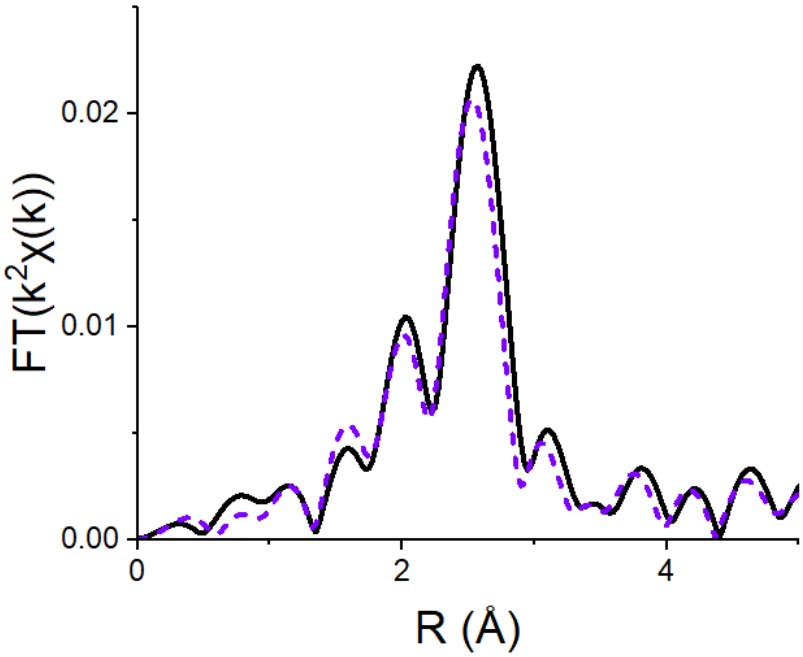

Figure S11. k^2-weighthed Fourier transform of the Pd K edge EXAFS spectra of the 0.5 wt% Ti containing catalyst reduced at 550 °C (black, solid) then oxidized at 30 °C (purple, dash)

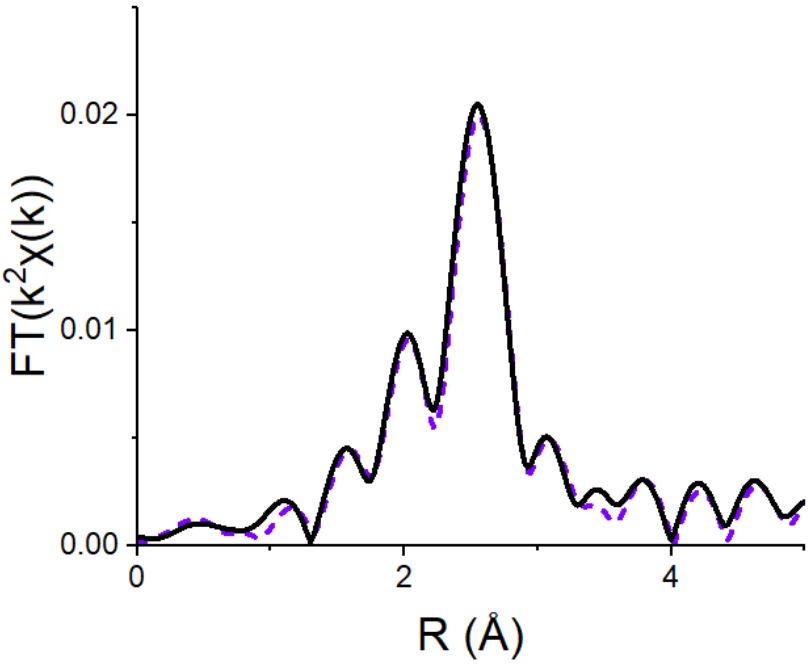

Figure S12. k^2-weighthed Fourier transform of the Pd K edge EXAFS spectra of the 1.0 wt% Ti containing catalyst reduced at 550 °C (black, solid) then oxidized at 30 °C (purple, dash)

Table S5 includes the catalytic rates that were used to calculate the coverages in Figure 8.

Table S5. Coverage of 0.5 wt% Ti containing catalyst after reduction at 550 °C, oxidation at different temperatures, and re-reduction at 200 °C

Oxidation Temperature (°C)	**Rate (mol C_3H_8*mol_{metal}^{-1}*s^{-1})**	**Coverage (%)**
-	0.8	75
30	1.1	63
200	1.6	48
300	2.0	35
350	3.0	0
400	3.1	0

Table S6 includes the EXAFS fits of all catalysts after 450 °C calcination, 550 °C reduction, and 30/200/300/350° C oxidation. All had similar peaks characteristic of Pd and PdO. There is increasing peak height and area of the PdO peak as oxidation temperature is increased for all catalysts which indicates increasing PdO coordination and an increased fraction of Pd oxidized.

Table S6. EXAFS fits of catalysts reduced at 550 °C then oxidized at different temperatures

Ti Loading (wt%)	Oxidation Temperature (°C)	Scattering Path	CN	R (Å)	$\Delta\sigma^2$ (Å^2)	E_o Shift (eV)	Fraction Pd Oxidized
0	30	Pd-Pd	4.0	2.72	0.0040	-1.3	0.60
		Pd-O	2.4	2.03	0.0020	2.2	
	200	Pd-Pd	2.5	2.72	0.0040	0.2	0.65
		Pd-O	2.6	2.03	0.0020	2.4	
	300	Pd-Pd	1.9	2.72	0.0040	0.8	0.75
		Pd-O	3.0	2.03	0.0020	1.4	
	350	Pd-Pd	1.0	2.72	0.0040	-1.8	0.80
		Pd-O	3.2	2.02	0.0020	3.1	
0.1	30	Pd-Pd	5.5	2.72	0.0040	-1.4	0.28
		Pd-O	1.1	2.04	0.0020	-1.9	
	200	Pd-Pd	4.7	2.72	0.0040	-0.2	0.35
		Pd-O	1.4	2.03	0.0020	-1.2	
	300	Pd-Pd	3.7	2.72	0.0040	-1.1	0.65
		Pd-O	2.6	2.022	0.0020	1.7	
	350	Pd-Pd	0.9	2.72	0.0040	-2.2	0.75
		Pd-O	3.0	2.04	0.0020	2.1	
0.5	30	Pd-Pd	6.3	2.72	0.0040	-1.3	0.15
		Pd-O	0.5	2.04	0.0020	1.4	
	200	Pd-Pd	5.0	2.73	0.0040	0.4	0.35
		Pd-O	1.4	2.02	0.0020	-0.7	
	300	Pd-Pd	3.6	2.72	0.0040	-0.2	0.53
		Pd-O	2.1	2.03	0.0020	-2.3	
	350	Pd-Pd	2.2	2.72	0.0040	1.4	0.68
		Pd-O	2.7	2.03	0.0020	2.6	
1.0	30	Pd-Pd	6.5	2.73	0.0040	-0.4	0.13
		Pd-O	0.5	2.03	0.0020	2.2	
	200	Pd-Pd	4.2	2.72	0.0040	0.3	0.33
		Pd-O	1.3	2.02	0.0020	-1.6	
	300	Pd-Pd	3.3	2.72	0.0040	-0.4	0.48
		Pd-O	1.9	2.02	0.0020	0.8	
	350	Pd-Pd	2.5	2.72	0.0040	-2.8	0.63
		Pd-O	2.5	2.02	0.0020	-1.6	

Table S7 includes the catalytic rates used to calculate the coverages in Figure 10.

Table S7. Coverage of SMSI catalysts after calcination at 450 °C, reduction at 550 °C, oxidation at 350 °C, and re-reduction at different temperatures

Ti Loading (wt%)	Re-reduction Temperature (°C)	Rate (mol C_3H_8*mol_{metal}^{-1}*s^{-1})	Coverage (%)
0.1	200	2.7	0
	300	2.5	7
	400	2.3	16
	500	1.8	34
	550	1.6	40
0.5	200	3.1	0
	300	2.0	27
	400	1.3	55
	500	0.9	70
	550	0.8	73
1.0	200	2.7	0
	300	1.4	47
	400	0.8	72
	500	0.4	87
	550	0.4	84

PUBLICATIONS

Breckner, C.; Zhu, K.; Wang, M.; Zhang, G.; Li, C. W.; Miller, J. T.; "Controlled site coverage of strong metal-support interaction (SMSI) on Pd NP catalysts," *Catal. Sci. Technol.*, 13, 157-169, 2023.

Breckner, C. J.; Pham, H. N.; Dempsey, M. G.; Perez-Ahuatl, M. A.; Kohl, A. C.; Lytle, C. N.; Datye, A. K.; Miller, J. T.; "The role of Lewis acid sites in γ-Al_2O_3 oligomerization," *ChemPhysChem*, Submitted 2023.

Yan, Q.; Simmons, T. R.; Cordell, W. T.; Lozada, N. J. H.; **Breckner, C. J.**; Chen, X.; Jindra, M. A.; Pfleger, B. F.; "Metabolic engineering of β-oxidation to leverage thioesterases for production of 2-heptanone, 2-nonanone and 2-undecanone," *MBE*, 61, 335-343, 2020.

Ma, R.; Gao, J.; Dean, D.; **Breckner, C.**; Liang, K.; Zhou, B.; Miller, J.; Zou, G.; "Insights into the Nature of Selective Nickel Sites on Ni/Al_2O_3 Catalysts for Propane Dehydrogenation," *ACS Catal.*, 12, 12607-12616, 2022.

Zelinsky, R.; Dean, D. P.; **Breckner, C. J.**; Miller, J. T.; Epling, W. S.; "Pd/BEA Hydrocarbon Traps: Effect of Hydrothermal Aging on Trapping Properties and Pd Speciation," *Appl. Catal. B*, 320, 121938, 2023.

Jacobs, H. P.; Elias, W. C.; Heck, K. N.; Dean, D. P.; Zhang, W.; Arredondo, J. H.; **Breckner, C. J.**; Hong, K.; Botello, C. R.; Chen, L.; Mueller, S. G.; Alexander, S. R.; Miller, J. T.; Wong, M. S.; "Impregnation of KOAc on PdAu/SiO_2 causes Pd-acetate formation and metal restructuring," *J. Mater. Chem. A*, 11, 6918-6933, 2023.

Bian, K.; Zhang, G.; Wang, M.; Liu, S.; **Breckner, C. J.**; Dean, D. P.; Zhu, J.; Miller, J. T.; Hou, S.; Song, C.; Guo, X.; "Promoting propane dehydrogenation over PtFe bimetallic catalysts by optimizing the state of Fe species," *Chem. Eng. Sci.*, 275, 118748, 2023.

Turnley, J. W.; Deshmukh, S. D.; Boulos, V. M.; Spilker, R.; **Breckner, C.**; Ng, K.; Liu, J. K.; Miller, J. T.; Kenttämaa, H. I.; Agrawal, R.; "A Selenium-Based "Alkahest": Reactive Dissolutions of Metals and Metal Compounds with Alkylammonium Polyselenide Solutions," *Inorg. Chem. Front.*, Accepted 2023.